Mitogen-activated protein kinase activity drives cell trajectories in colorectal cancer

Florian Uhlitz[1,2,3,*], Philip Bischoff[1,4,*], Stefan Peidli[1,2,*], Anja Sieber[1,2], Benedikt Obermayer[5], Eric Blanc[5], Alexandra Trinks[1,4], Mareen Lüthen[1,3], Yana Ruchiy[1], Thomas Sell[1,2], Soulafa Mamlouk[1,3], Roberto Arsie[6], Tzu-Ting Wei[6], Kathleen Klotz-Noack[1,7], Roland F Schwarz[3,6], Birgit Sawitzki[7], Carsten Kamphues[3,8], Dieter Beule[5], Markus Landthaler[4,6], Christine Sers[1,3,4], David Horst[1,3,4], Nils Blüthgen[1,2,3,4,#] and Markus Morkel[1,3,4,#]

1 Charité Universitätsmedizin Berlin, Corporate Member of Freie Universität Berlin, Humboldt-Universität zu Berlin, and Berlin Institute of Health, Institute of Pathology, Charitéplatz 1, 10117 Berlin, Germany

2 IRI Life Sciences, Humboldt University of Berlin, Philippstrasse 13, 10115 Berlin, Germany

3 German Cancer Consortium (DKTK) Partner Site Berlin, German Cancer Research Center (DKFZ), 69120 Heidelberg, Germany

4 Berlin Institute of Health (BIH), Anna-Louisa-Karsch-Straße 2, 10178 Berlin, Germany

5 Charité Universitätsmedizin Berlin, Corporate Member of Freie Universität Berlin, Humboldt-Universität zu Berlin, and Berlin Institute of Health, Core Unit Bioinformatics (CUBI), Charitéplatz 1, 10117 Berlin, Germany

6 Berlin Institute for Medical Systems Biology (BIMSB), Max Delbrück Center for Molecular Medicine, Hannoversche Strasse 28, 10117 Berlin, Germany

7 Charité Universitätsmedizin Berlin, Corporate Member of Freie Universität Berlin, Humboldt-Universität zu Berlin, and Berlin Institute of Health, Institute of Medical Immunology, Augustenburger Platz 1, 13353 Berlin

8 Charité Universitätsmedizin Berlin, Corporate Member of Freie Universität Berlin, Humboldt-Universität zu Berlin, and Berlin Institute of Health, Department of Surgery, Hindenburgdamm 30, 12203 Berlin

[*] joint first authors

[#]corresponding authors: markus.morkel@charite.de, Tel: ++49-30-450 536 107; nils.bluethgen@charite.de, Tel: ++49-30-2093 92 390

Abstract

In colorectal cancer, oncogenic mutations transform a hierarchically organized and homeostatic epithelium into invasive cancer tissue lacking visible organization. We sought to define colorectal cancer cell types and signals controlling their development. More than 30,000 epithelial single cell transcriptomes of tumors and matched non-cancerous tissues of twelve colorectal cancer patients were clustered into six patient-overarching groups defined by differential activities of oncogenic signaling pathways such as mitogen-activated protein kinase and oncogenic traits such as replication stress. RNA metabolic labeling and assessment of RNA velocity in patient-derived organoids revealed developmental trajectories of colorectal cancer cells organized along a mitogen-activated protein kinase activity gradient. This was in contrast to normal colon organoid cells developing along graded Wnt activity. Experimental targeting of EGFR-BRAF-MEK in cancer organoids affected signaling and gene expression contingent on predictive KRAS/BRAF mutations and induced cell plasticity overriding default developmental trajectories, providing a basis for non-genetic resistance to targeted therapies.

Keywords: Cancer profiling / ERK / RNA velocity / Single Cell RNA Sequencing / SLAM-Seq

48 **Introduction**

49 Healthy cells in the human body develop along trajectories controlled by intrinsic and extrinsic signals
50 to ensure tissue homeostasis. Cancer cells cannot maintain homeostasis, as oncogenic mutations
51 activate signaling pathways cell-intrinsically and render cancer cells unresponsive to paracrine signals
52 (Hanahan & Weinberg, 2011). Colorectal cancer (CRC) commonly initiates via mutations activating
53 Wnt/β-catenin signaling that maintains stem cells in the normal colon epithelium (Fearon, 2011).
54 Subsequent mutations deregulate further signaling pathways such as RAS-RAF-MEK-ERK (also known
55 as mitogen-activated protein kinase; MAPK signaling) providing pro-proliferative cues. Less frequently,
56 CRC initiates via BRAF mutations, or from chronic inflammation increasing the mutation rate in the
57 tissue (De Palma *et al*, 2019; Lasry *et al*, 2016). Genetic CRC drivers have direct and indirect effects on
58 cancer cell development and the cellular composition of CRC and its microenvironment.

59 There is substantial evidence for the existence of tumor cell subpopulations and clonal architecture in
60 CRC depending on genetics, microenvironmental cues, and space constraints (Van Der Heijden *et al*,
61 2019). Cancer stem cells are defined by their capacity for self-renewal and ability to initiate clonal
62 outgrowth (Kreso & Dick, 2014). CRC cells with these characteristics have been distinguished by surface
63 proteins like CD133, EPHB2 or LGR5 (Ricci-Vitiani *et al*, 2007; O'Brien *et al*, 2007; Merlos-Suárez *et al*,
64 2011). Likewise, lineage tracing in CRC cancer models has revealed preferential outgrowth of cancer
65 cell subpopulations defined by expression of genes such as *LGR5* or *IL17RB* (Goto *et al*, 2019;
66 Shimokawa *et al*, 2017) or by localization at the leading edge of the tumor (Lamprecht *et al*, 2017).
67 Furthermore, it has been shown that CRC cells at the invasive front expressing genes such as the matrix
68 metalloproteinase MMP7 contribute disproportionally to metastasis (Brabletz *et al*, 1999; Vermeulen
69 *et al*, 2010). While these studies suggest that CRC cells are heterogeneous and hierarchically organized,
70 other studies stress that developmental capacities of CRC cells are subject to a high degree of plasticity.
71 In particular, oncogenic mutations and paracrine signals have been shown to trigger reversal of
72 developmental trajectories so that differentiated cells regain stem cell characteristics (Schwitalla *et al*,
73 2013; Buczacki *et al*, 2013; Jadhav *et al*, 2017).

74 CRC is treated by chemotherapy and/or therapies targeting MAPK signaling, depending on predictive
75 mutation status. Patients with metastatic CRC without RAS or RAF mutations profit from anti-EGFR
76 antibody therapy (Van Cutsem *et al*, 2009; Karapetis *et al*, 2008), while patients with BRAF-mutant CRC
77 now receive first-line therapy combinations of anti-EGFR antibodies and BRAF kinase inhibitors
78 (Corcoran *et al*, 2018). Recent studies suggest roles for cell plasticity in therapy resistance. For instance,
79 chemoresistance has been linked to subpopulations of CRC cells expressing the transcription factor
80 ZEB2 (Francescangeli *et al*, 2020), and acquired anti-EGFR therapy resistance has been associated with
81 stromal remodeling (Woolston *et al*, 2019).

82 Taken together, emerging evidence suggests that hierarchically organized tumor cell heterogeneity
83 and cell plasticity play key roles in CRC progression and therapy response. However, developmental
84 states of CRC cell are not well defined, and it is not known whether distinct differentiation states form
85 preferential developmental trajectories. Here, we use single-cell RNA sequencing to identify patient-
86 overarching CRC cell types defined by strengths of oncogenic signals and replicative responses. We use
87 metabolic labelling of RNA in CRC organoids to delineate CRC development and show that CRC cell
88 differentiation states, developmental trajectories and therapy-associated cell plasticity are informed
89 by MAPK activity.

90

91

92 **Results**

93 CRC cells can assume distinct patient-overarching states

94 To capture the diversity of CRC cell states compared to the normal colon epithelium, we performed
95 single-cell transcriptome analysis of twelve previously untreated CRC patients undergoing primary
96 surgery (Fig. 1A). We utilized tissue samples that included the invasive tumor front and matched
97 adjacent non-cancerous tissues (Supplementary Fig. 1). Tumors encompassed stages pTis (Tumor *in*
98 *situ*) to pT4, with or without metastasis, and with various locations along the cephalocaudal axis of the
99 colon (Supplementary table 1). Genetic analysis revealed mutational patterns characteristic for
100 canonical CRC progression in most tumors; however, tumors from patients P007, P014, P020 and P026
101 contained the $BRAF^{V600E}$ mutation often associated with the serrated progression pathway and tumor
102 P008 was colitis-associated (Supplementary tables 1, 2). Eleven Patients were diagnosed with
103 microsatellite-stable (MSS) CRC, while patient P026 was microsatellite-instable (MSI). We produced
104 transcriptome libraries using a commercial droplet-based system and sequenced the libraries to obtain
105 transcriptomes covering 500 to 5000 genes per cell. Transcriptomes were clustered and clusters were
106 allocated to epithelial, immune or stromal subsets, using known marker genes (Smillie *et al*, 2019) (Fig.
107 1B, Supplementary Fig. 2, Supplementary table 3), and more than 30,000 epithelial cell transcriptomes
108 were analyzed further.

109 Epithelial cell transcriptomes of the different patients largely intermingled when visualized in a
110 standard UMAP embedding employing ten principal components (McInnes *et al*, 2018), but partially
111 separated when using a higher number of 50 components for UMAP embedding, particularly in areas
112 enriched for tumor-derived transcriptomes (Fig. 1C). This suggests the existence of patient-specific
113 gene expression patterns in cancer epithelium, but not in normal colon tissue. In summary, the UMAP
114 embedding indicates that our single cell data are largely free from sample-specific bias, but instead
115 reflect intrinsic differences between normal and tumor cell transcriptomes.

116 We used cell type-specific signatures and marker genes to annotate the epithelial cell clusters (Smillie
117 *et al*, 2019; Fig. 1D, E, Figure EV1, Supplementary table 2). In the normal epithelium, we identified stem
118 cells by markers such as *LGR5* and *OLFM4*. Neighboring clusters were annotated as enterocyte
119 progenitors or mature enterocytes by expression of absorptive lineage markers such as *KRT20* and
120 *FABP1* (Supplementary Fig. 3, Supplementary table 3). *BEST4*- and *OTOP2*-expressing enterocytes
121 formed a discrete cluster (Parikh *et al*, 2019). Further separate epithelial clusters were identified as
122 immature and mature secretory goblet cells expressing *MUC2* and *TFF3,* and as tuft cells expressing
123 *TRPM5.* In tumor tissue, we additionally identified four tumor-specific clusters, termed TC1-TC4. These
124 clusters were defined by high, but also unequal, levels of stem cell markers such as *OLFM4*, *CD44* and

125 *EPHB2* and DNA repair genes such as *XRCC2*. *MMP7* was among the few genes expressed exclusively
126 in the TC1-4 clusters, but not in the normal epithelium (Supplementary Fig. 3, Supplementary table 4).
127 Clusters populated by differentiated absorptive and secretory cells were reduced in tumors, and
128 profiles representing tuft cells and *BEST4*/*OTOP2*-positive enterocytes were vastly underrepresented.

129 MSS CRC is defined by somatic copy-number aberrations (SCNAs). Thus, we next distinguished cancer
130 from non-cancer cells in the tumor tissues by inferring SCNAs from the single cell transcriptome data.
131 We identified clusters of SCN-aberrant epithelial cells in ten out of the twelve tumors (Fig. 1F, Fig.
132 EV2A). Exome sequencing of tumors P007, P008 and P009 validated SCNA calling from transcriptomes,
133 showing that the procedure is robust for our single cell data (Fig. EV2B). P014 and P026 contained no
134 cells with overt SCNAs. This was expected for tumor P026, which is MSI and thus defined by single
135 nucleotide polymorphisms rather than SCNAs, but unexpected for P014, which was diagnosed as BRAF-
136 mutant however MSS. In-depth analysis of patient-specific gene expression patterns (Supplementary
137 Fig. 4A) and protein distributions (Supplementary Fig. 4B) revealed that patient-specific differences in
138 cancer cell transcriptomes are at least partly driven by individual patterns of genomic gains and losses
139 (Supplementary Fig. 4C-E, Supplementary table 5).

140 More than 86% of the TC1-4 cells were called SCN aberrant, along with substantial fractions of cells
141 defined as stem cell/TA-like (36%) or immature goblet cells (22%, Fig. 1F, G). In contrast, a large
142 majority (95%) of mature absorptive enterocytes and mature goblet cells derived from tumor samples
143 were identified as copy number normal, and therefore likely stem from non-cancerous tissue at the
144 tumor margins. In summary, our analyses define normal stem/TA-like cells, immature goblet-like cells,
145 and TC1-4 cells as six main patient-overarching clusters of CRC cells.

146

147 Epithelial tumor cell clusters differ by oncogenic traits and signals

148 We next defined characteristics of the six CRC cell clusters by assessing relative strengths of
149 transcriptional footprints related to oncogenic signaling and cancer-associated functional traits (Fig.
150 2A, B). TC1 and TC4 were significantly enriched for the expression of direct ERK targets that are
151 activated by MAPK (P=0.004 and P=0.006, FDR-corrected post-hoc Wilcox tests, respectively; Schubert
152 *et al*, 2018), across all tumors and in particular in P007. We furthermore found a strong association of
153 TC1 cells with the expression of hallmark signatures related to DNA repair and the G2/M replication
154 checkpoint across all individual cancers (P=1.4E-10; Liberzon *et al*, 2015). This indicates that TC1 cluster
155 cancer cells experience high levels of replication stress, a therapy-relevant trait of many cancers,
156 including CRC. Indeed, TC1 cluster cells were exclusively assigned to the S or G2/M cell cycle phases by
157 gene expression (Fig. 2C), in line with cells under replication stress, as also seen by *XRCC2* expression

158 (Supplementary Fig. 3). The DNA damage-associated protein PARP stained many nuclei of the TC1-high
159 CRC tissue P009 but not of TC1-low P008 (Fig. 2D). Cancer cells clustered in TC4 were characterized by
160 expression of an intestinal YAP target signature (P=2.2E-8; Serra *et al*, 2019). YAP transcriptional
161 activity is linked to regenerative responses and tumor progression (Zanconato *et al*, 2016). TC2
162 transcriptomes were significantly associated with high PI3K pathway activity (p=8.9E-10), related to
163 control of metabolism and apoptosis. Wnt/β-catenin target gene activity was high across all TC
164 clusters, but stem/TA-cell-like cancer cells showed stronger expression of a LGR5-ISC stem cell
165 signature that is Wnt-driven (Merlos-Suárez *et al*, 2011; Muñoz *et al*, 2012), but this association was
166 not significant across the patients. In summary, assessment of cell signaling signatures provides
167 information on pathway activities of epithelial cancer cell clusters, and specific features of individual
168 tumors. The analyses indicate that assignment of cancer cell transcriptomes to the TC1-4 clusters
169 reflects, at least partially, differential states of oncogenic networks and oncogene-induced functional
170 traits.

171

172 RNA metabolic labeling defines tumor cell hierarchies that correlate with MAPK activity

173 Immunofluorescent staining of primary CRC sections with antibodies directed against the stem cell
174 marker OLFM4, the proliferation marker KI67 and the differentiation markers TFF3 and FABP1 revealed
175 cell heterogeneity, but not how cancer cells in the tissue are related to each other (Fig. EV3). To
176 establish whether CRC cells are hierarchically organized, we established organoid lines of two tumor
177 samples, P009 and P013 (Fig. 3A). Organoids matched the cancer tissue on a mutational level
178 (Supplementary Table 1). We cultured the cancer organoids, termed P009T and P013T, as well as
179 normal colon organoids, termed NCO, in medium containing Wnt, R-Spondin, and EGF (WRE medium)
180 or alternatively in medium lacking Wnt and R-Spondin (E medium). NCO organoids cultured in WRE
181 medium showed graded expression of the intestinal LGR5-ISC stem cell signature, while expression of
182 differentiation markers was graded in the opposite direction (Fig. 3B). LGR5-ISC signature activity was
183 lost when NCO organoids were cultured in E medium. In P009T and P013T CRC organoids, LGR5-ISC
184 signature activity was higher and independent of Wnt/R-Spondin, while expression of differentiation
185 signature genes was much lower. Taken together, these expression patterns are in line with Wnt-
186 dependent stem cell maintenance in normal tissue, and Wnt-independent stem cell maintenance and
187 block of terminal differentiation in cancer tissue with APC mutations. The data however do not show
188 whether graded developmental trajectories exist in CRC.

189 We, therefore, metabolically labelled RNAs of the organoids by 4-thio-uridine, before dissociation and
190 single cell sequencing (scSLAM-Seq; Fig. 3C) (Herzog *et al*, 2017; Jürges *et al*, 2018). This allowed us to

191 distinguish nascent labelled from older non-labelled mRNA, to order cells along inferred latent time
192 based on dynamic RNA expression (Bergen *et al*, 2020), also known as RNA velocity (Supplementary
193 Fig. 5 for quality controls). When cultured in WRE medium, developmental trajectories of normal NCO
194 organoids initiated in areas of maximal LGR5-ISC signature scores and terminated in a region
195 containing differentiated cells (Fig. 3D). When cultured without Wnt/R-Spondin in E medium, NCO
196 normal colon organoids lost uniform direction of RNA velocity. In contrast, the P009T and P013T cancer
197 organoids maintained strong transcriptional trajectories regardless of Wnt/R-Spondin in the medium.

198 We ordered organoid transcriptomes along latent time and assessed strengths of oncogenic signals
199 (Fig. 3E). In line with the key role of Wnt in stem cell maintenance, normal colon organoids showed a
200 gradient of Wnt/β-catenin target gene expression along latent time when cultured in WRE medium. In
201 contrast, both P009T and P013T cancer organoids showed no graded Wnt/β-catenin-related
202 expression, but a clear gradient of MAPK target gene activity along latent time in both medium
203 conditions. *TFF3*, marking secretory differentiation, was graded in CRC organoids along latent time,
204 but *FABP1*, marking absorptive differentiation in the normal colon, was not (Fig. 3F), in line with *TFF3*
205 marking goblet-like CRC cells at the end of developmental trajectories. Proliferation marker *MKI67* was
206 confined to the beginning of the latent time trajectory of normal organoids in WRE medium and
207 showed extended gradients in CRC organoids. Both P009T and P013T organoids displayed Wnt-
208 dependent loss of *MKI67* expression along latent time and also Wnt-dependent *MMP7* expression. In
209 summary, our metabolic RNA labelling experiments indicate decreasing MAPK activity along CRC
210 developmental trajectories and suggests a role for Wnt as a paracrine signal influencing gene
211 expression, such as *MMP7*, in APC-deficient CRC cells.

212

213 MAPK target gene expression defines CRC differentiation states

214 As MAPK-related gene expression was associated with developmental trajectories in CRC organoids,
215 we analyzed whether the previously defined states of primary CRC cells are organized along a MAPK
216 gradient in primary CRC. We assigned the SCN-aberrant primary cancer cell transcriptomes to 40 bins
217 along a gradient of diminishing LGR5-ISC gene signature activity or along decreasing MAPK activity,
218 and determined expression levels of the stem cell markers *LGR5* and *EPHB2* (Merlos-Suárez *et al*, 2011)
219 (Fig. 4A). As expected, both *LGR5* and *EPHB2* were graded with LGR5-ISC signature strength; but
220 expression of the MAPK target gene signature also ordered tumor cells in agreement with both CRC
221 cell hierarchy markers and performed even better in sorting cells along a gradient of *EPHB2* expression.
222 We conclude that expression patterns of known CRC cell hierarchy markers are in agreement with
223 MAPK-driven development.

224 When ordering primary CRC transcriptomes along a gradient of LGR5-ISC activity, a higher proportion
225 of stem/TA-like tumor cells aggregated at the high end of the gradient, whereas tumor cells assigned
226 as immature goblet cell-like accumulated in the lower end, and TC1-4 cells displayed a broad
227 distribution (Fig. 4B). In contrast, ordering of CRC cells by MAPK signature activity significantly enriched
228 TC1 and TC4 cells at the start of the gradient (P=8.6E-23 and P=7.6E-20, respectively, adjusted
229 Pearson´s chi-squared p-value), whereas stem/TA- and immature goblet cell-like cells concentrated at
230 the lower end (P=1.3E-19 and P=1.1E-8, respectively). These aggregate differences were also reflected
231 in cell state distributions of individual patients (Fig. 4C): P007 showed the highest MAPK activity, and
232 the highest proportion of TC4 cells which clustered disproportionally in the MAPK-high bins. TC1 and
233 TC4 cells had also the highest average MAPK activities in most other CRCs, including P008, P012, P013,
234 and P016. In contrast, stem-/TA-like tumor cells and immature goblet-like CRC cells displayed relatively
235 low expression of MAPK targets in all tumors, particularly in P009, P012, P013 P017, P021, P025 and
236 P008, P017, respectively.

237 To experimentally determine whether the CRC cell states are functionally linked to MAPK activity, we
238 blocked MAPK signaling in CRC organoids by the MEK1/2 inhibitor Selumetinib (AZD6244) or by
239 Selumetinib in combination with the EGFR inhibitor Sapatinib (AZD8931) and analyzed singe cell gene
240 expression after 48h (Fig. 4D). We found that cells showing a high TC1 signature were diminished after
241 MEK inhibition in P009T organoids, while the fraction of cells with a high goblet-like signature was
242 increased. Likewise, P013T organoid cells showed lower expression of the TC4 signature genes after
243 MAPK blockade, and higher expression of the stem cell-related LGR5-ISC signature. These results
244 suggest that CRC cell states are MAPK-driven.

245

246 Targeted therapy alters cell signaling networks and differentiation signatures in CRC organoids

247 MAPK is a key target of CRC therapy, as blockade of EGFR is the first-line therapy for patients with
248 metastasized MAPK-wildtype CRC, and combined blockade of EGFR and BRAF is first-line therapy for
249 patients with advanced CRC containing oncogenic BRAF mutations. We therefore asked whether
250 targeted therapy is associated with changes in CRC cell states and trajectories. In addition to the
251 RAS/RAF-wildtype organoid lines P009T and P013T, we employed OT227 and OT302 organoids carrying
252 $KRAS^{G13D}$ and $KRAS^{G12V}$ mutations, respectively, and the $BRAF^{V600E}$-mutant lines B2040 and C2019. As
253 the clinically relevant blockade of EGFR using the antibody Cetuximab was not effective *in vitro* as also
254 observed by others (Schütte *et al*, 2017), we treated the organoids with the EGFR inhibitor Sapatinib,
255 the BRAF inhibitor LGX818 (Encorafenib), the MEK inhibitor Selumetinib and combinations for 48h,
256 before subjecting single cell suspensions to CyTOF and scSLAM-seq (Fig. 5A, Supplementary Fig. 6 for

257 summaries of CyTOF data) to measure relative activities of signal transducers and related
258 transcriptional signatures, respectively (Fig. 5B).

259 The effects of inhibitor treatments on the signaling network were variable between lines, but we also
260 observed communalities between the lines with shared RAS/RAF mutational status (Fig. 5C). In
261 RAS/RAF-wildtype lines, treatment with EGFR inhibitor reduced both MEK and ERK phosphorylation.
262 MEK inhibition decreased ERK phosphorylation, but increased MEK phosphorylation via negative
263 feedback suppression (Fritsche-Guenther *et al*, 2011). BRAF inhibitors increased levels of MEK and ERK
264 phosphorylation, suggesting paradoxical activation of RAF (Hatzivassiliou *et al*, 2010). In contrast, the
265 KRAS-mutant lines OT227 and OT302 were largely unresponsive to EGFR inhibition, while MEK
266 inhibition caused strong upregulation of MEK phosphorylation, and BRAF blockade strongly
267 upregulated both MEK and ERK phosphorylation. A similar response to MEK inhibition was found in
268 the BRAF-mutant lines C0219 and B2040, however in these lines BRAF inhibition alone or in
269 combination with EGFR inhibition resulted in substantial loss of ERK phosphorylation. Across all lines,
270 we observed a positive correlation between phosphorylation of ERK and the Ki67 ($P<0.005$, using linear
271 models with line-specific offsets) and a negative correlation between p-ERK and cleaved Caspase3
272 ($P<0.005$) and cleaved PARP levels, in line with roles of MAPK in activation of proliferation and
273 inhibition of apoptosis.

274 Furthermore, we found high correlation between ERK phosphorylation and expression of MAPK target
275 genes ($P<0.0001$, using linear models with line-specific offsets; Fig. 5D, E), between p-ERK and YAP
276 protein levels ($P<0.0001$), and between MAPK target expression and YAP target expression ($P<0.0001$).
277 In contrast, MAPK target activity was negatively correlated with Wnt target activity (and $P<0.05$,
278 respectively; Fig. 5E). A direct interaction between MAPK and YAP signaling is supported by induction
279 of transgenic $BRAF^{V600E}$ in a mouse intestinal organoid model (Riemer *et al*, 2015), which resulted not
280 only in activation of the MAPK target gene signature, but also in an even stronger activation of YAP
281 target genes (Fig. 5F). Our findings thus indicate that the MAPK, YAP and Wnt signaling pathways form
282 an interconnected network controlling transcription, and ultimately proliferation and cell fate in CRC.
283 Accordingly, we found that experimental inhibition of MAPK also modulated prevalence of cell-type-
284 related signatures (Fig. 5D): in P013T, OT227 and B2040 organoid lines, effective repression of ERK
285 phosphorylation was correlated with activation of the LGR5-ISC stem cell-related signature, while gene
286 expression related to the MAPK-high cell states TC1 and TC4 was downregulated under these
287 conditions in all lines.

288

289

290 Targeted therapy alters developmental trajectories of CRC organoid cells

291 For a detailed analysis of CRC cell development under experimental MAPK therapy, we assessed
292 transcriptome data on single cell level. Anti-MAPK therapy had broad consequences on gene
293 expression, as transcriptomes derived from conditions of effective ERK suppression often inhabited
294 different spaces in a UMAP representation (Fig. 6A), as quantified by hierarchical clustering of
295 conditions based on a similarity matrix of shared neighboring cells (Fig. 6B). We found that inhibition
296 of EGFR, alone or in combination with BRAF or MEK inhibition, was effective in the induction of
297 transcriptome changes in MAPK-wildtype organoids. Likewise, a combination of BRAF and EGFR
298 inhibitors deregulated transcriptomes effectively in the BRAF-mutant organoid B2040, while both
299 inhibitors were not as effective on their own. BRAF-mutant C2019 organoids were largely unresponsive
300 to anti-MAPK treatment. As also observed for ERK phosphorylation (Fig. 5C, above), these effects agree
301 with clinical reality, where positive outcomes for EGFR and combinatorial BRAF/EGFR inhibition are
302 variable but limited to patients with RAS/RAF wildtype and BRAF-mutant CRC, respectively.

303 We next assessed developmental trajectories, by computing dynamical cell velocity and latent time
304 from scSLAM data. Cells of five out of six organoid lines developed along a MAPK gradient, and one
305 line, OT227, did not show any preferential direction of cell development as assessed by RNA velocity
306 (Fig. EV4A). The LGR5-ISC Wnt-driven stem cell signature marked the start of cell trajectories only in
307 the BRAF-mutant lines. Except for OT227, developmental trajectories ended with increased goblet cell-
308 like gene expression.

309 We next analyzed developmental trajectories in P013T organoids, comparing control and the clinically
310 relevant anti-EGFR treatment conditions (Fig. 6C, D). Comparison of dynamical cell velocities indicated
311 that the formerly uniform developmental trajectory along the MAPK gradient became divergent after
312 EGFR inhibitor treatment, with one group of CRC cells developing towards an endpoint similar to
313 unperturbed growth (Fig. 6D, red arrow 1), while the remaining cells formed opposite trajectories (Fig.
314 6D, red arrow 2). Cycling cells in G2/S were diminished across the complete UMAP space inhabited by
315 EGFR inhibitor-treated cells (Fig 6E). The former developmental endpoint 1 was characterized by goblet
316 cell differentiation, including the goblet cell marker TFF3 and apoptosis signatures (Fig 6F), while the
317 latter endpoint 2 was characterized by high LGR5-ISC expression. Accordingly, endpoint 2 showed *de-*
318 *novo* expression of the Wnt target *AXIN2* as indicated by the dynamics in the phase plot after EGFR
319 inhibition (Fig. 6G), and also by the more restricted fields of expression (also termed moments) for the
320 older non-labelled as compared to the newer labelled RNAs (Fig. 6H). These patterns are strong
321 indications for the re-routing of cell development towards a state high in expression of Wnt-driven
322 stem cell gene expression and agree with organoid culture showing slow outgrowth of resistant P013T
323 colonies under long-term EGFR treatment (Fig. EV5).

324 We also observed characteristic changes in directed cell development after MAPK inhibition in most
325 other CRC organoid lines (Fig. EV4B-D). RAS/RAF-wildtype P009T organoid cells likewise developed
326 towards a state of increased LGR5-ISC-related gene expression after EGFR inhibition (Fig. EV4B). KRAS-
327 mutant OT227 organoid cells, while displaying no clear trajectories in the absence of treatment,
328 formed two streams of preferred trajectories after 48h of MEK inhibition, ending in regions of G1-
329 arrested cells with active LGR5-ISC, differentiation and apoptosis transcriptome signatures (Fig. EV4C).
330 In contrast, trajectories of OT302 organoid cells under MEK inhibition headed towards a region defined
331 by goblet cell-like differentiation and apoptosis with decreased LGR5-ISC-related gene expression (Fig.
332 EV4D). BRAF-mutant B2040 organoid cells developed towards a differentiation/apoptosis high
333 trajectory endpoint under control conditions, but towards a LGR5-ISC-high state under combined
334 EGFR/BRAF inhibition (Fig. EV10E). Taken together, in most lines examined, we observed separation of
335 transcriptomes in the UMAP between control and effective treatment conditions, as a result of gene
336 expression changes that can be interpreted as a re-routing of cell developmental trajectories towards
337 endpoints defined either by differentiation followed by apoptosis, or by the induction of LGR5-ISC
338 related gene expression characteristic for intestinal stem cells.

339

340

341 **Discussion**

342 Here, we provide a comprehensive analysis of patient-overarching states of CRC cells forming
343 developmental trajectories (Fig. 6 I). We define six clusters comprising cells resembling normal
344 stem/TA cells, goblet cell-like tumor cells, and clusters TC1-4 that were largely confined to tumor
345 tissue. The TC1-4 clusters were defined by differential activities of oncogenic pathways, including
346 MAPK. We find that cell hierarchies in CRC are organized along developmental trajectories following
347 MAPK gradients. In combination, the analyses imply that CRC cells develop along transient
348 developmental states rather than forming fixed cell populations in organoids and probably also in
349 patients. As cell state prevalence differed between patients, we suggest that CRC cell trajectories are
350 guided and constrained by individual cancer genome characteristics such as patterns of oncogenic
351 driver mutations. Our experiments in organoids indicate that therapies targeting the MAPK pathway
352 reduce proliferation, but also redirect developmental trajectories of CRC cells towards goblet-cell
353 differentiation-like apoptotic or Wnt-driven stem-cell like endpoints that could be associated with
354 therapy-sensitivity or resistance, respectively. In summary, our analysis provides a single cell-based
355 framework for cell plasticity during cancer development and targeted therapy.

356 Previous single cell studies defined features of the CRC immune microenvironment (James *et al*, 2020;
357 Zhang *et al*, 2020; Lee *et al*, 2020); however, no consensus exists on patient-overarching features
358 defining cells of the epithelial CRC compartment. Here, we define key states of CRC cells that are
359 products of differential oncogene-associated signals resulting in distinctive transcriptomes. Our
360 analyses suggest that CRC cells with lower levels of MAPK activity can resemble normal stem cells
361 characterized by high expression of Wnt-driven LGR5-ISC signature genes (van de Wetering *et al*, 2002;
362 Merlos-Suárez *et al*, 2011). However, individual stem cell markers such as *OLFM4* or *CD44* were
363 expressed even stronger in the tumor-specific TC1-4 clusters. Based on these transcriptional patterns,
364 it appears that no unique stem cell signature exists in CRC and that Wnt, YAP and MAPK activities
365 together can maintain different cell states that may act as functional equivalents of stem cells that can
366 sustain tissue growth. A recent study identified ribosomal transcription and protein translation as a
367 key determinator of CRC stemness (Morral *et al*, 2020); this model agrees with our data, as ribosomal
368 genes were overrepresented among the top-scoring genes determining the MAPK-driven trajectories
369 described here (see Supplementary Fig. 5B for an example).

370 MAPK is a key pathway for targeted therapy, as many CRC patients profit from anti-EGFR or anti-
371 EGFR/anti-BRAF therapy (Karapetis *et al*, 2008; Amado *et al*, 2008; Kopetz *et al*, 2019). By and large,
372 outcomes of our experimental inhibition of MAPK in organoids agreed with known relationships
373 between predictive mutations and therapy sensitivity, as EGFR inhibition was only effective in MAPK-
374 wildtype organoids, while a combination of BRAF and EGFR inhibitors – but not each inhibitor alone –

375 had profound effects on development of BRAF^{V600E}-mutant CRC organoids. In addition, we show that
376 graded MAPK-driven gene expression drives differentiation trajectories, as inferred from RNA velocity
377 after MAPK inhibition in CRC organoids, extending our previous finding of graded ERK activity in CRC
378 organoids (Brandt *et al*, 2019). In combination, these findings suggest that intrinsic resistance to anti-
379 MAPK therapies may rely on re-routing of developmental trajectories of CRC cells. Indeed, the ability
380 to reverse developmental trajectories in the intestinal epithelium has been found before (Schwitalla
381 *et al*, 2013; Buczacki *et al*, 2013; Jadhav *et al*, 2017). Our study therefore adds new aspects to current
382 models of anti-MAPK therapy resistance defined by cell plasticity (Woolston *et al*, 2019; Misale *et al*,
383 2014).

384 Importantly our study suggests that multiple signaling pathways form a therapy-relevant
385 interconnected network of oncogenic signaling pathways in CRC. For instance, we find that YAP and
386 MAPK levels are positively correlated on the protein activity and the transcriptional response levels.
387 YAP maintains regenerative responses and is a key driver of CRC and other cancers (Zanconato *et al*,
388 2016). In contrast, MAPK and Wnt signaling were negatively correlated. We and others previously
389 showed loss of Wnt-driven intestinal stem cells by high MAPK levels provided by oncogenic BRAF
390 (Riemer *et al*, 2015; Tong *et al*, 2017). Here, we find that therapeutic inactivation of MAPK can result
391 in Wnt and LGR5-ISC signature reactivation, in agreement with a previous study (Zhan *et al*, 2019). As
392 both pathways, Wnt and MAPK, are generally activated by oncogenic mutations in CRC, cross-inhibition
393 between the pathways would mean that therapeutical suppression of one pathway results in
394 oncogene-driven activation of the other, possibly explaining why many therapeutic approaches to
395 block MAPK proved insufficient in the clinic. It will be an important goal for future studies to identify
396 combinations of actionable signals that can be exploited for therapies resulting in uniform
397 commitment of CRC cells to differentiation-related and apoptotic endpoints instead of re-routing
398 subsets of cancer cells towards stem cell-like states.

399 Our study also identified further cancer traits in CRC cell clusters with relevance to therapy. For
400 instance, TC1 cells were defined by high levels of replication stress, which can be functionally
401 associated with high MAPK activity (Sheu *et al*, 2012; Klotz-Noack *et al*, 2020).Tumors with high TC1
402 cell content were strongly positive for PARP, an important therapeutic target (Sun *et al*, 2020). It is of
403 note that the CMS subtyping system developed for bulk tissue CRC transcriptomes (Guinney *et al*,
404 2015) could not distinguish the CRC cell types that we identified here on the single cell level, as most
405 epithelial cancer cells were assigned to CMS1 or CMS2 with the exception of goblet-like cells that can
406 adopt CMS3 (Supplementary Fig. 7).

407 In addition to patient-overarching CRC cell traits, we also observed patient-specific gene expression
408 differences. Our integrated analysis of single cell transcriptomes and copy number gains and losses

409 indicated that patient-specific gene expression patterns were significantly associated with copy
410 number gains that we inferred from transcriptomes and validated using exome sequencing of three
411 patients. On another level, we observed patient-specific gene expression patterns that translated into
412 regional patterns of proteins, as evidenced by the staining for MMP7 which was confined to the
413 invasive front of some tumors. Such patterns of gene activity and protein translation indicate that
414 tumor cell development is highly plastic and partly regulated by immune and stromal cells in the
415 microenvironment. Thus, we expect that the intrinsic developmental paths of CRC cells that we
416 observe in organoid cultures are modulated by extrinsic cues from the microenvironment *in vivo*.
417 Future studies using co-cultures of different tumor-associated cell types could disentangle key
418 paracrine relationships in cancer.

419 We analyzed here primary cancer epithelium and organoid transcriptomes. Novel single cell
420 approaches, taking into account the diversity of the tumor microenvironment in patient cohorts
421 stratified by treatment, complex cell culture models, the extension of single-cell analyses to multi-
422 omics, and the preservation of spatial information at a cellular level promise to identify cellular
423 heterogeneity and genetic diversity of cancer at even greater detail in the future. The combination of
424 such approaches has the potential to improve the molecular understanding of cancer and therapy
425 prediction for patients (Rajewsky *et al*, 2020). Our work defining developmental trajectories of CRC
426 contributes to this goal.

427

428 **Materials and Methods**

429 **Collection and single-cell RNA sequencing of clinical specimens**

430 Fresh normal colon and colorectal cancer tissues were acquired during the intraoperative pathologist´s
431 examination at Charité University Hospital Berlin. Tissues (approx. 0.1-0.4g) were minced using
432 scalpels, processed using the Miltenyi Human Tumor Dissociation Kit (Miltenyi, #130-095-929) and a
433 Miltenyi gentleMACS Tissue Dissociator (Miltenyi, #130-096-427), using program 37C_h_TDK_1 for 30-
434 45min. For three tumors, we also used digestion with the cold active protease from Bacillus
435 licheniformis (Sigma P5380) at approx. 6°C for 45min. with frequent agitation, following a published
436 protocol (Adam *et al*, 2017) (Supplementary Fig 8). Cell suspensions were filtered using 100µm filters,
437 pelleted by centrifugation, treated with 1ml ACK erythrocyte lysis buffer, washed and resuspended in
438 ice-cold PBS, and filtered using 20µm filters. Debris was removed using the Debris Removal Solution
439 (Miltenyi #130-109-398). Cell suspensions were analyzed for cell viability >75% using LIVE/DEAD
440 Fixable Dead Cell Stain Kit (488nm; Thermo Fisher) and a BD Accuri cytometer. 10.000 single cells were
441 used for single-cell library production, using the Chromium Single Cell 3´Reagent Kits v3 and the
442 Chromium Controller (10x Genomics). Libraries were sequenced on a HiSeq 4000 Sequencer (Illumina)
443 at 200-400mio. reads per library to a mean library saturation of approx. 50%. This resulted in 35.000
444 to 120.000 reads per cell.

445 **DNA Sequencing**

446 For panel sequencing, DNA was extracted from FFPE tumor tissue using the Maxwell RSC DNA FFPE Kit
447 (Promega) or the GeneRead DNA FFPE kit (Qiagen) and sequenced using a CRC panel (Mamlouk *et al*,
448 2017), and/or the Ion AmpliSeq Cancer Hotspot Panel (CHP) v2 and an IonTorrent sequencer
449 (ThermoFisher). Variant calling was performed using Sequence Pilot (Version 4.4.0, JSI Medical
450 Systems) or SoFIA (Mamlouk *et al*, 2017). For exome sequencing, DNA was isolated from fresh frozen
451 tumor tissue using the DNeasy Blood and Tissue Kit (Qiagen). Exomes were sequenced using the
452 AllExon Human SureSelect v7 Kit (Agilent).

453 **Histology and immunostaining**

454 3-5 µm tissue sections of formalin-fixed and paraffin-embedded (FFPE) tissue were used.
455 Immunostainings were performed on the BenchMark XT immunostainer (Ventana Medical Systems),
456 using CC1 mild buffer or Ultra CC1 buffer (Ventana Medical Systems) for 30 min at 100°C, and using
457 antibodies rabbit anti-TFF3 (1:250, Abcam, ab108599), mouse anti-FABP1 (1:1000, Abcam, ab7366),
458 rabbit anti-OLFM4 (1:100, Atlas Antibodies, HPA077718), mouse anti-EPCAM (1:100, ThermoScientific,
459 MS-144-P1), rabbit anti-Ki67 (1:400, Abcam, ab16667), mouse anti-Ki67 (1:50, Dako, M7240), rabbit
460 anti-LYZ (1:1500, Abcam, ab108508), rabbit anti-EREG (1:50, Thermo Fischer Scientific, PA5-24727),

461 anti-PARP1, mouse anti-MUC2 (1:50, Leica, NCL-MUC-2), mouse anti-CK17 (1:10, Dako, M7046),
462 mouse anti-MMP7 (1:100, ThermoFisherScientific, MA5-14215). Images were taken using AxioVert.A1
463 (Zeiss) or CQ1 (Yokogawa) microscopes or scanned using the Pannoramic SCAN 150 scanner
464 (3DHISTECH).

465 **Organoid culture and metabolic labelling**

466 Tumor cells were washed in Advanced DMEM/F12 medium (Gibco), embedded in Matrigel, and
467 cultured in 24-well plates, as published (Sato *et al*, 2011). Wnt3 and R-Spondin3 were prepared as
468 conditioned media (Sato *et al*, 2011). For single-cell sequencing, organoids were dissociated
469 completely using TrypLE and DNAseI, and filtered via a 20µm filter. For single cell SLAM-seq, NCO,
470 P009T and P013T replicate cultures were cultured in media with and without Wnt/R-Spondin, and
471 P009T, P013T, OT227, OT302, B2040, C2019 organoids were cultured in standard media (Sato *et al*,
472 2011; Schütte *et al*, 2017) with DMSO, or were treated for 48 with 100nM AZD8931 (Sapatinib), 100nM
473 LGX818 (Encorafenib) and/or 8µM AZD6244 (Selumetinib). Organoids were metabolically labelled in
474 culture using 200µM 4-thio-uridine for 2 h (Herzog *et al*, 2017), harvested, disaggregated to single cells
475 by TrypLE, and fixed in fixation buffer (80% methanol/20% DPBS) at ≥ -20° C. Samples were warmed to
476 room temperature and incubated with 10mM iodoacetamide. Alkylation was carried out overnight, in
477 the dark, with gentle rotation, followed by two washes with cold fixation buffer. Single cell suspensions
478 were rehydrated and incubated 10 minutes at room temperature in 100mM DTT. Samples were
479 resuspended in fixation buffer and conserved at -80 °C.

480 **Mass Cytometry (CyTOF)**

481 For CyTOF analysis, we used a panel of antibodies described in Brandt *et al*, 2019, and measurements
482 were performed essentially as in described in the same publication. In short, organoids were harvested
483 in PBS and digested to a single cell solution in 1:1 Accutase (Biolegend) and TrypLE (Gibco) with addition
484 of 100 U/ml Universal Nuclease (Thermo Scientific) at 37°C. Cells were counted and a maximum of
485 500.000 cells were stained with 5 µM Cell-ID Cisplatin (Fluidigm) in PBS for 5 min at 37°C, washed in
486 PBS, resuspended in medium and incubated for 30 min at 37°C, resuspended in BSA/PBS solution,
487 mixed 1:1.4 with Proteomics Stabilizer (Smart Tube Inc.) and frozen at -80°C for storage.

488 For analysis, cells were thawed, mixed with Maxpar Cell Staining Buffer (CSB, Fluidigm), labelled using
489 the Cell-ID 20-Plex Pd Barcoding Kit, and washed again in CSB, then in Barcode Perm Buffer (Fluidigm).
490 After barcoding, cells were pooled and stained with a surface antibody cocktail, as described previously
491 (Brandt *et al*, 2019). Data was acquired on a Helios CyTOF system. Mass cytometry data was normalized
492 using the Helios software and bead-related events were removed. Doublets were excluded by filtering
493 for DNA content (^{191}Ir and ^{193}Ir) vs. event length, and apoptotic debris removed by a filter in the platin

494 channel (^{195}Pt). De-convolution of the barcoded sample was performed using the CATALYST R package
495 version 1.5.3 (Chevrier *et al*, 2018).

496

497 **Primary tissue single-cell RNA-seq data analysis**

498 UMIs were quantified using cellranger 3.0.2 with reference transcriptome GRCh38. Spliced, unspliced
499 and ambiguous UMIs were quantified with velocyto (La Manno *et al*, 2018) (mode: run10x, default
500 parameters). For parameters and initial quality controls, see Supplementary Fig. 2. Epithelium, stromal,
501 and immune cells were identified by scoring cell type markers across Louvain clusters for each sample
502 (resolution = 1). Cell type markers used to score epithelium, stromal, and immune cells were adapted
503 from Similie et al. (Smillie *et al*, 2019) and are listed in Supplementary table 3. Sample-wise quality
504 control assessments and subsettings into main cell types are documented at sys-bio.net/sccrc/.
505 Normalized subsets were merged for each main cell type of normal and tumor samples without further
506 batch correction.

507 SNN graph, Louvain clusters and UMAP embeddings were recomputed for each subset based on top
508 ten components. Louvain cluster-specific marker genes of merged normal and tumor samples were
509 used to identify sub cell types among epithelial, stromal and immune subsets. Here, marker genes
510 were determined with Seurat (Stuart *et al*, 2019)(wilcox text) at a minimum log fold change threshold
511 of 0.25. Gene expression sets were taken from the hallmark signature collection of the Broad institute
512 (Liberzon *et al*, 2015), unless otherwise referenced in the main text, and were scored as implemented
513 in the progeny R package and Seurat v3, respectively.

514 For copy-number assessment, InferCNV v1.3.3 was used with default parameters. Copy number
515 aberrant clones were cut at k = 2 in inferCNV dendrograms. Clone-wise SCNA scores were computed
516 by calculating the average standard deviation in inferCNV expression of all cells and divided by the
517 average standard deviation in inferCNV expression of all normal samples taken together. Clones with
518 a SCNA score greater than the highest observed score for normal samples were considered copy
519 number aberrant.

520 **Organoid single-cell RNA-seq data analysis**

521 Single cell SLAM sequencing data was pre-processed using cellranger v4.0, and labeled and unlabeled
522 reads were counted using the alignments (as BAM files), using a custom pipeline utilizing Snakemake
523 (Köster & Rahmann, 2012), SeqAn (Döring *et al*, 2008), R. For each read, the numbers of T nucleotides
524 and T-to-C conversions was counted, leaving out positions with common SNPs (using the dbSNP build
525 151 as available as track from UCSC genome browser). For each molecule as identified by cell barcode

526 and UMI, positions with discordant nucleotides were excluded. Subsequently, molecules were counted
527 as nascent RNA if they contained a T-to-C conversion, and old RNA otherwise.

528 scRNAseq and scSLAM-seq data for organoids was analyzed using scanpy (Wolf *et al*, 2018)and scvelo
529 (Bergen *et al*, 2020). For diffusion map analysis and RNA velocity, cells were first filtered by the number
530 of genes (between 2000 and 5000) and the percent mitochondrial reads (between 0.075 and 0.2) and
531 normalized, using scvelo standard settings. Cell cycle was scored according to the scanpy standards.
532 Cell cycle was scored based on a list of cell cycle associated genes (Kowalczyk *et al*, 2015). Resulting
533 S_score, G2M_score and UMI counts per cell were regressed out. The diffusion map was calculated on
534 the top 10 components and using a neighborhood graph with 50 neighbors and calculated on all genes.
535 UMAP embeddings were computed based on a PCA on only the 2000 most highly variable genes
536 obtained with scanpy. The similarity measure between conditions in Figure 6B was defined by the
537 average fraction of shared neighbors in a nearest neighbor graph over all cells in the dataset, then
538 performing hierarchical clustering on the resulting similarity matrix.

539 Moments were calculated on 30 principal components and 30 neighbors separately per condition in
540 order to avoid smoothing effects between different conditions within the same dataset. Velocity was
541 calculated using the dynamical model from scvelo on 2000 most highly variable genes according to
542 scanpy, which were then filtered for at least 20 shared counts in both SLAM layers. Furthermore, for
543 most of the captured genes in the first perturbation experiment we observed either induced or
544 repressed gene dynamics only. Such one-sided dynamics proved ambiguous to fit kinetics to, since at
545 least two local maxima of model likelihood are possible. In order to resolve this ambiguity, we modified
546 the dynamical model from scvelo with an additional regularization term. This term introduces prior
547 information to the model by penalizing the number of cells that are assigned a higher latent time than
548 a given set root priors. Before fitting we inferred the root cells in a data-driven manner as those ten
549 cells with the stem cell signature. An additional initialization of each gene model with restricted
550 parameters ensured that both local minima were actually captured. When fitting the second
551 perturbation experiment datasets we did not observe any benefit when imposing a prior, hence
552 continued without one.

553 **Ethics permission**

554 All patients were aware of the planned research and agreed to the use of tissue. Research was
555 approved by vote EA4/164/19 of the ethic´s commission of Charité - Universitätsmedizin Berlin.

556 **Data availability**

557 Scripts for processing of patient tissue scRNA sequencing data are available from
558 https://github.com/molsysbio/sccrc. Scripts for processing of organoid RNA velocity data are available

559 from https://github.com/molsysbio/sccrc_slamvelocity. Raw data is stored in GEO under the accession
560 numbers GSE166555 (patient data) und GSE166556 (organoid data). Processed count data is available
561 from https://sys-bio.net/sccrc.

562

563

Acknowledgements

The work was in part funded by Berlin Institute of Health (PB, NB, CS, DH and MM), German Cancer Consortium DKTK (NB, MM), Deutsche Forschungsgemeinschaft (MM, grant MO2783/5), DFG research training group (SP and TTW, grant GRK2424/1), BMBF (NB), and the Helmholtz Association (RFS).

Author contributions

PB, FU, SP, MM, AS, MLu, AT, TS, RA, YR, SM, KKN conducted and analyzed experiments; FU, SP, NB, BO, EB, TTW performed bioinformatic analyses; MM, NB, PB, CS, DB, BS, DH, MLa, RFS conceived, designed, interpreted experiments and/or supervised parts of the study; PB, MM, DH, CK, AT contributed to clinical sample acquisition and preparation; MM wrote the manuscript; all authors provided critical feedback and helped shaping the research, analysis, and manuscript.

Conflicts of interest

The authors declare no conflicts of interest

The Paper Explained

PROBLEM

Cancer cells, like normal cells in our bodies, are thought to develop along preferred trajectories. It is unknown which signals control development of colorectal cancer cells, and how cancer therapies interfere with such signals.

RESULTS

We find that colorectal cancer cells develop along trajectories defined by activity of a signaling pathway termed MAPK, which is also a clinically important target for therapy. We find that experimental therapies inactivating MAPK disturb development of colorectal cancer cells in culture, resulting in cancer cells heading towards an unwanted stem cell-like state. This cellular behavior might explain cases of therapy resistance observed in patients.

IMPACT

Knowledge of developmental routes of cancer cells is key for future improvement of targeted therapy to avoid resistance.

594 **Main Figures**

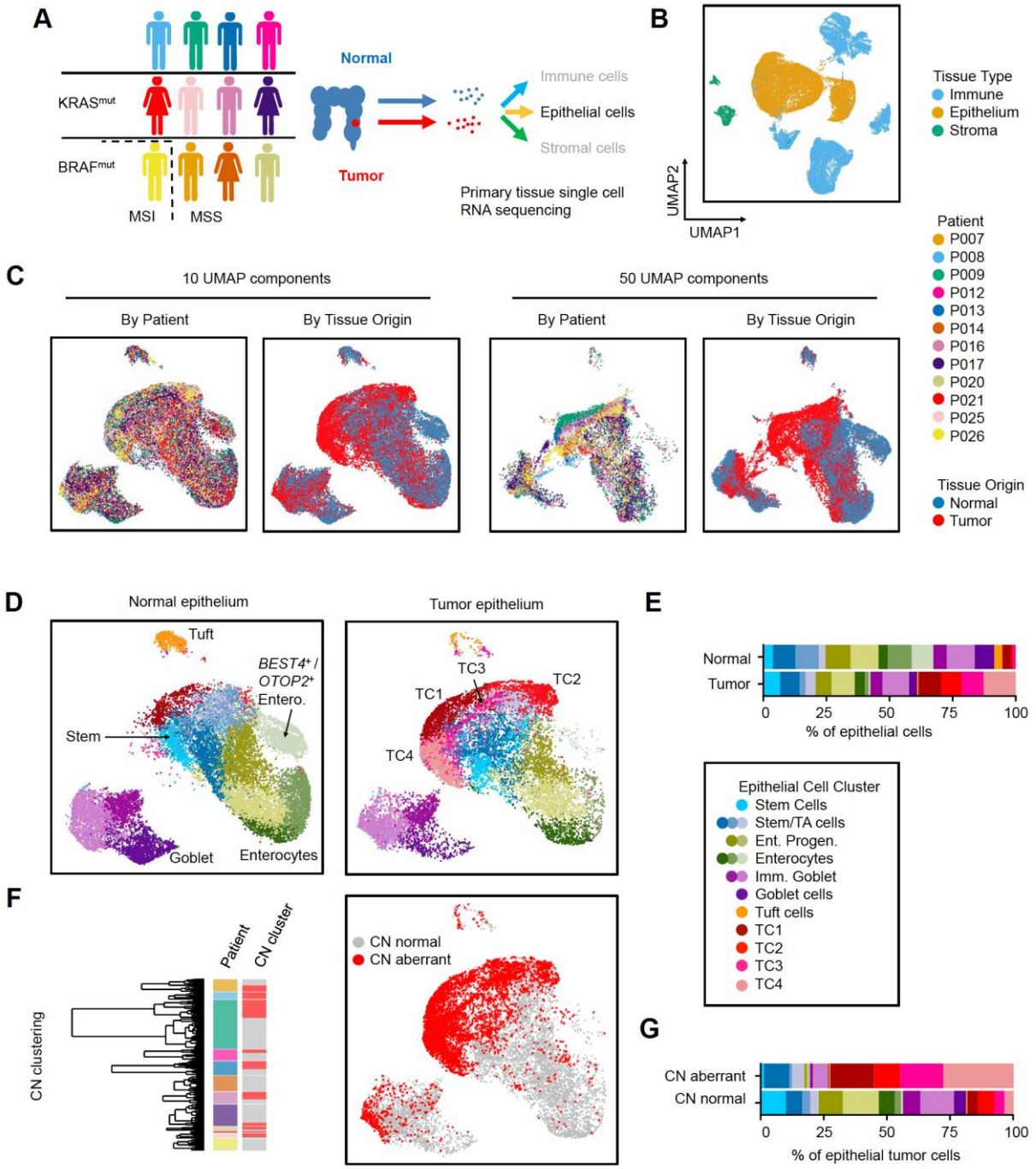

595

596

597 **Figure 1: Generation of CRC single-cell RNA sequencing data and epithelial cell type census. A**
598 Workflow of the Clinical Single Cell Sequencing pipeline. In short, CRC and adjacent non-tumor tissue
599 was sampled from 12 patients. Single cell RNA sequencing data was generated using the 10x Genomics
600 platform, as outlined in Methods. For histology, see Supplementary Fig. 1. For patient characteristics,
601 see Supplementary table 1, for mutational data, see Supplementary table 2. **B, C, D** UMAPs of single
602 cell transcriptome data. **B** UMAPs of epithelial, immune, and stromal cell transcriptomes, color-coded

603 by tissue origin as assessed by marker genes. For marker genes, see Supplementary table 3 **C** UMAPs
604 of epithelial cell transcriptomes, color-coded by patient identity or tissue of origin, as indicated. D
605 UMAPs of epithelial cells, separated by tissue of origin (normal vs. tumor). Clusters are color-coded by
606 cell identity, as inferred from marker genes as outlined in main text. For epithelial cell cluster marker
607 genes, see Supplementary table 4. **E** Relative fractions of epithelial cell types across all patients. For
608 fractions per patient, see Supplementary Figure 3. **F** Identification of copy-number aberrant versus
609 normal epithelial cells in tumor tissue. To the left: Cell cluster dendrogram, color-coded by patient and
610 by copy-number-associated clusters (n=2 per patient). Copy-number normal cluster: grey; copy
611 number-aberrant cluster: red. To the right: Distribution of SCN aberrant cells (red). For associated
612 heatmap of gene expression and cell type data, see Supplementary Fig. 4. **G** Cell type assignment for
613 SCN-normal versus -aberrant cells.

614

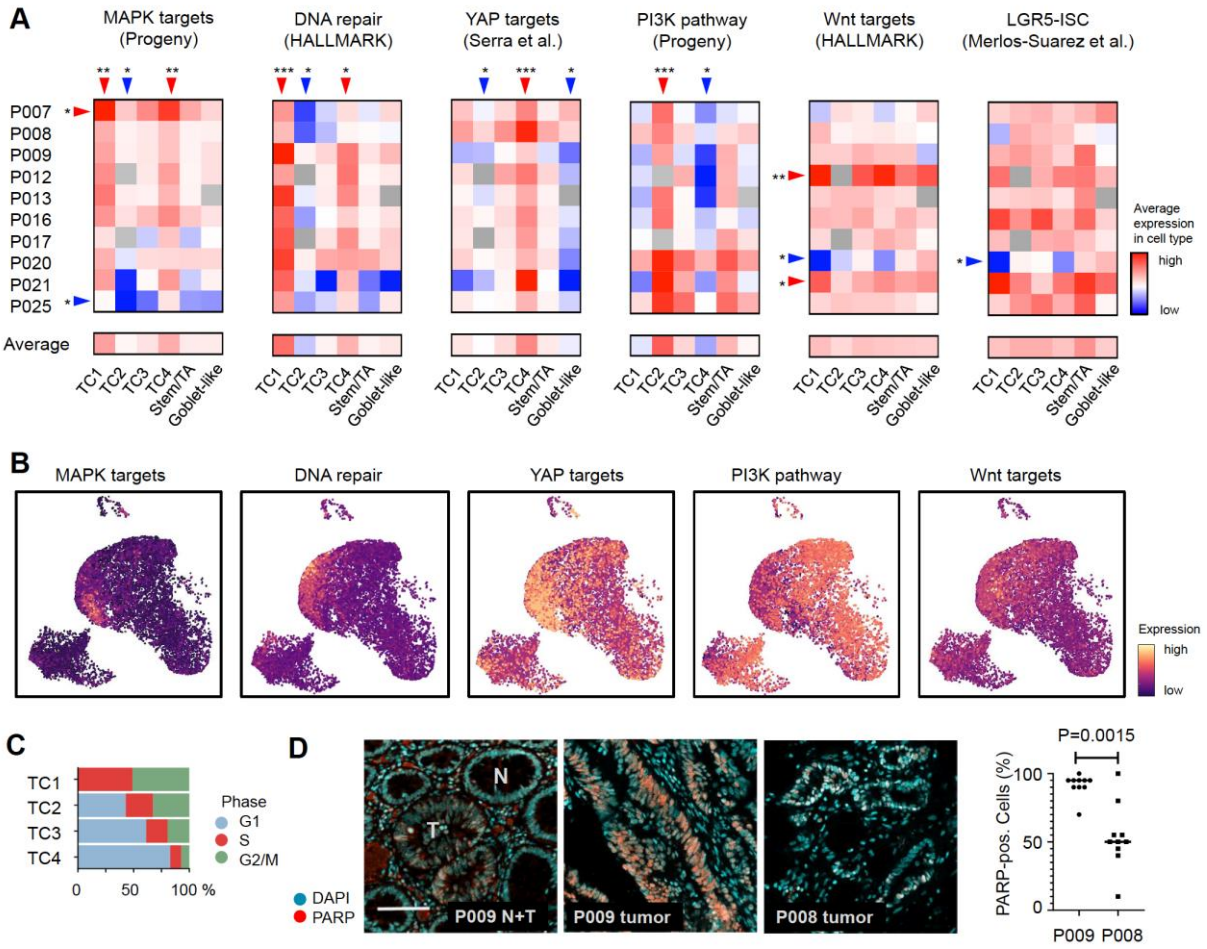

Figure 2. CRC cell clusters are distinguished by signaling pathway activities. **A** Transcriptional activity associated with key oncogenic traits and signals, by tumor-specific cell type and patient, as indicated. Red: High activity, blue: low activity. Significance was assessed by Kruskal Wallis Test (FDR corrected p<0.05), followed by a post-hoc analysis using a Wilcox-test of each group against all other groups, FDR corrected significance levels are shown (*=p<0.05; **=p<0.01; ***p<0.001). **B** Visualization of signatures corresponding to oncogenic traits and signals in the tumor cell transcriptome UMAP. **C** Cell cycle distribution of TC1-4 epithelial tumor cells, as inferred from single cell transcriptomes. **D** Immunofluorescence of DNA-damage-associated nuclear protein PARP. Images show adjacent normal and tumor crypts of tissue P009T, marked by N and T, respectively, and tumor tissue of patients P008 and P009, as indicated. Scale bar 100µm. Significance was assessed by an unpaired t-test, after blinded analysis of 10 random images per tumor.

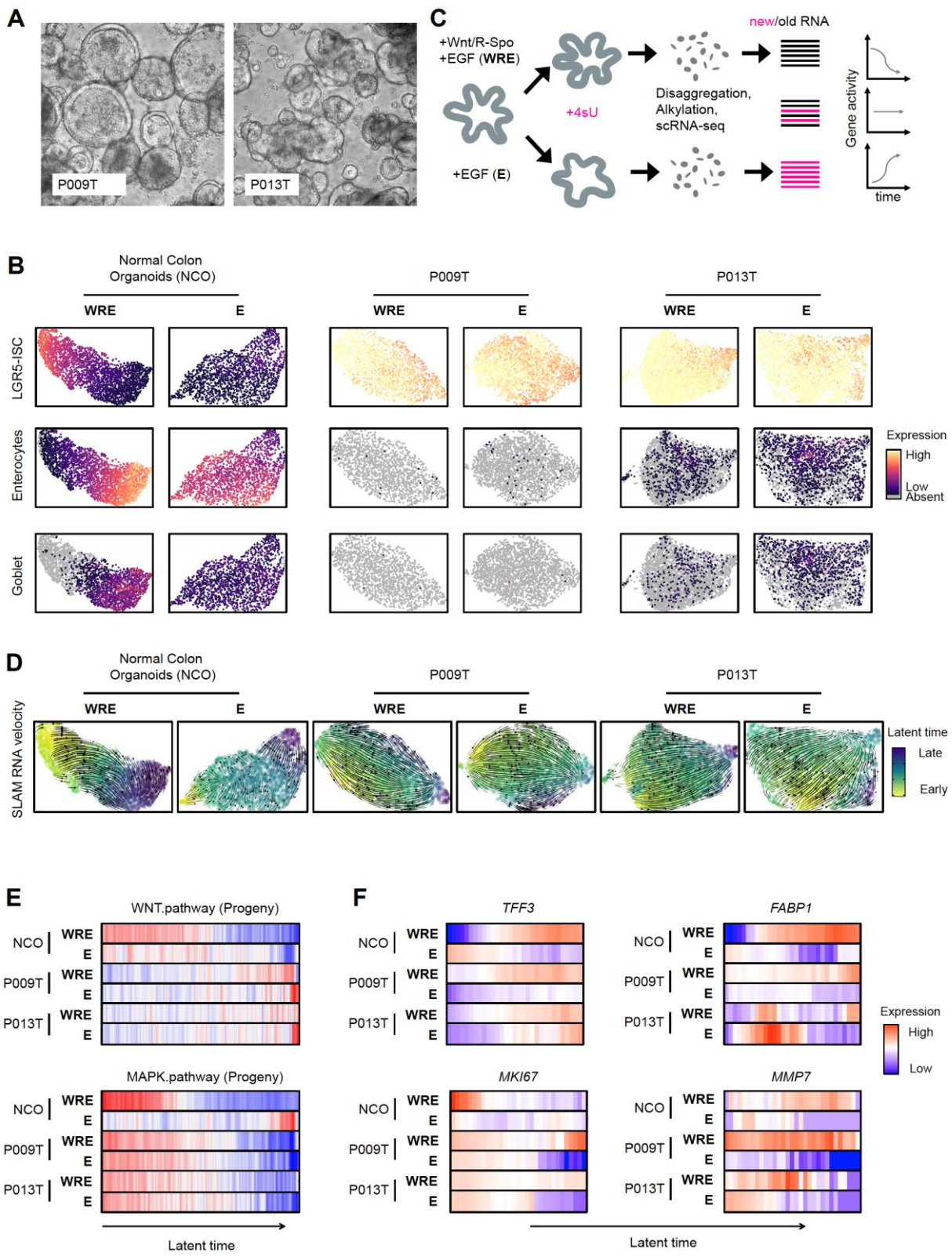

Figure 3: RNA metabolic labeling defines tumor cell trajectories in patient-derived organoids. **A** Phenotypes of patient-derived organoid lines P009T and P013T. **B** UMAPs of organoid single cell transcriptomes. Organoid lines and medium conditions as indicated. LGR5-ISC stem cell, enterocyte and Goblet cell signatures are visualized. **C** Schematic representation of SLAM-Seq workflow to infer RNA dynamics ("RNA velocity"). In short, organoids were passaged and assigned to different medium

634 conditions. After three days, nascent RNA was metabolically labelled for 2 h using 4sU. Organoids were
635 harvested, dissociated, and fixed. RNA in single cells was alkylated, and cells were subjected to single
636 cell sequencing. Reads were assigned to nascent or old RNA status, depending on diagnostic T-C
637 mutational status. **D** Developmental trajectories inferred from RNA metabolic labelling. Bold and thin
638 arrows indicate high versus low directionality of RNA velocity. Colors below RNA velocity show latent
639 time (yellow: early latent time; blue: late latent time). **E** Activities of Wnt/β-catenin and MAPK target
640 genes in organoid single cell transcriptomes, ordered along latent time. **F** Activities of *TFF3*, *FABP1*,
641 *MKI67* and *MMP7* in organoid single cell transcriptomes, ordered along latent time. Color code for
642 panels D-F: Red: high activity; blue: low activity.

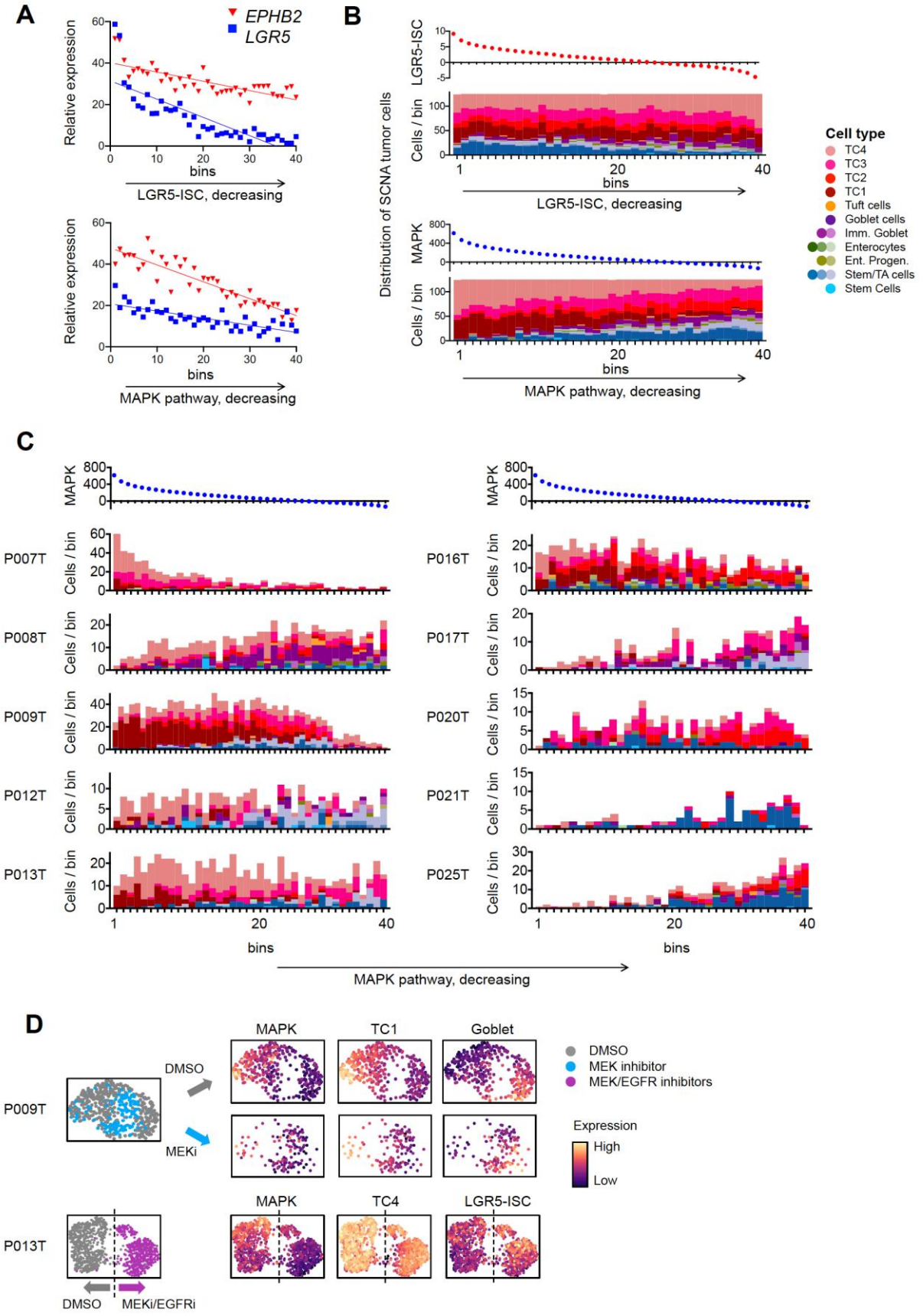
A
EPHB2
LGR5
Relative expression
bins
LGR5-ISC, decreasing
MAPK pathway, decreasing
B
LGR5-ISC
Cells / bin
MAPK
Distribution of SCNA tumor cells
LGR5-ISC, decreasing
MAPK pathway, decreasing
Cell type
TC4
TC3
TC2
TC1
Tuft cells
Goblet cells
Imm. Goblet
Enterocytes
Ent. Progen.
Stem/TA cells
Stem Cells
C
P007T
P008T
P009T
P012T
P013T
P016T
P017T
P020T
P021T
P025T
MAPK pathway, decreasing
D
MAPK
TC1
Goblet
TC4
LGR5-ISC
DMSO
MEKi
MEKi/EGFRi
DMSO
MEK inhibitor
MEK/EGFR inhibitors
Expression
High
Low

643

644

645 **Figure 4 (previous page): MAPK activity is linked to CRC cell differentiation states**. **A** Gene expression
646 of *LGR5* and *EPHB2*, along activity gradients of LGR5-ISC or MAPK target gene signatures. **B** Cell-type
647 distribution of SCN-aberrant CRC cells along gradients of LGR5-ISC or MAPK transcriptional signatures,
648 as in A. **C** Cell type distribution of SCN-aberrant CRC tumor cells along MAPK signature activity, as in B,
649 per tumor. Cell fractions are color-coded by cell identity, as in Fig. 1C. **D** UMAP representations of
650 single cell transcriptomes derived from P009T or P013T organoids, after MAPK blockade using MEK or
651 combined MEK and EGFR inhibition. Color codes are treatment conditions or signature strengths, as
652 indicated. Dashed line in P013T UMAP roughly separates control (DMSO) and MEK/EGFR inhibitor
653 treated cells.

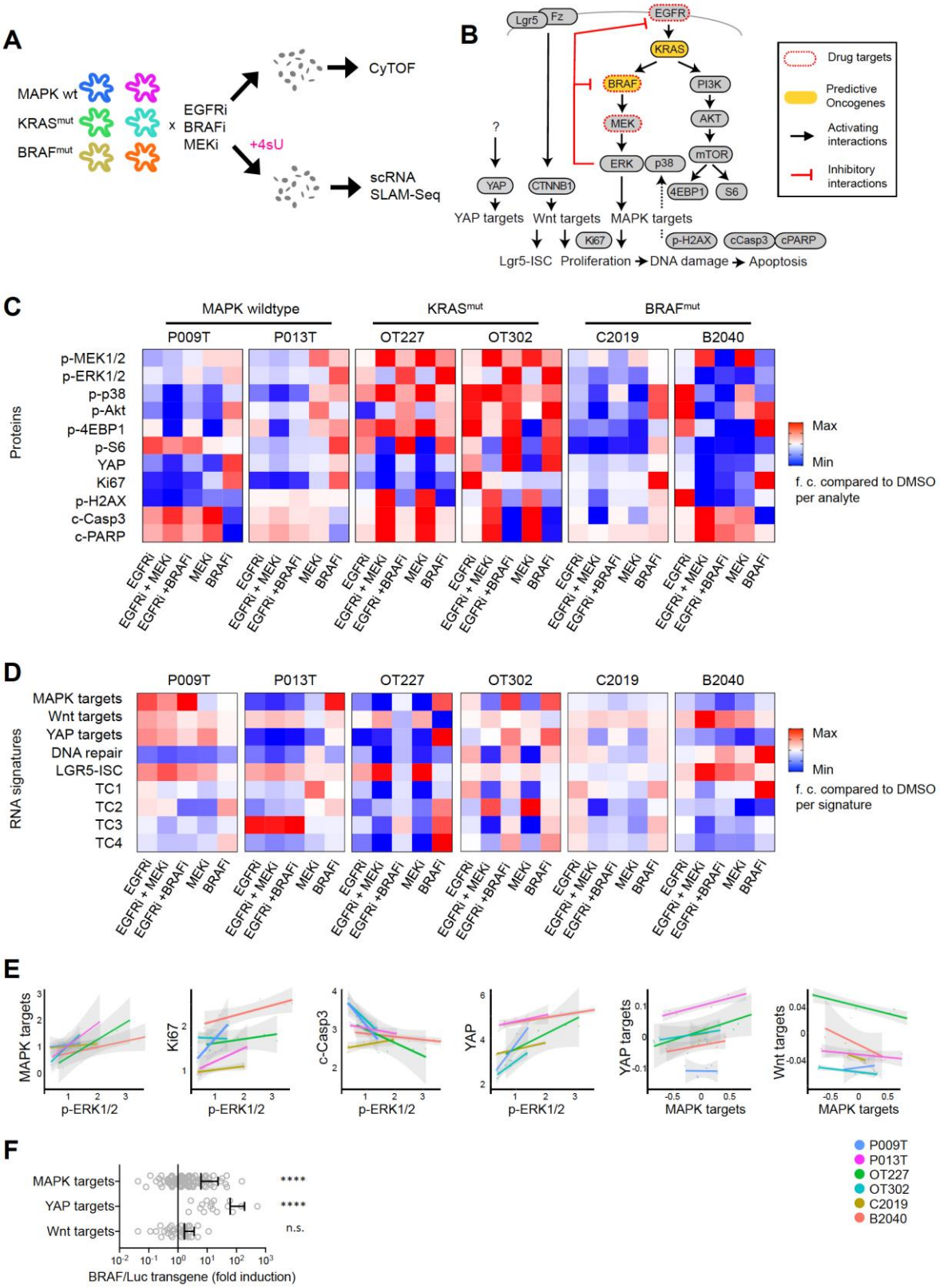
A
MAPK wt
KRASmut
BRAFmut
x
EGFRi
BRAFi
MEKi
+4sU
CyTOF
scRNA
SLAM-Seq
B
Lgr5
Fz
EGFR
KRAS
BRAF
PI3K
MEK
AKT
ERK
p38
mTOR
4EBP1
S6
YAP
CTNNB1
Ki67
p-H2AX
cCasp3
cPARP
YAP targets
Wnt targets
MAPK targets
Lgr5-ISC
Proliferation
DNA damage
Apoptosis
Drug targets
Predictive Oncogenes
Activating interactions
Inhibitory interactions
C
MAPK wildtype
KRASmut
BRAFmut
P009T
P013T
OT227
OT302
C2019
B2040
Proteins
p-MEK1/2
p-ERK1/2
p-p38
p-Akt
p-4EBP1
p-S6
YAP
Ki67
p-H2AX
c-Casp3
c-PARP
EGFRi
EGFRi + MEKi
EGFRi +BRAFi
MEKi
BRAFi
Max
Min
f. c. compared to DMSO per analyte
D
RNA signatures
MAPK targets
Wnt targets
YAP targets
DNA repair
LGR5-ISC
TC1
TC2
TC3
TC4
f. c. compared to DMSO per signature
E
MAPK targets
Ki67
c-Casp3
YAP
YAP targets
Wnt targets
p-ERK1/2
F
MAPK targets
YAP targets
Wnt targets
****
n.s.
BRAF/Luc transgene (fold induction)
P009T
P013T
OT227
OT302
C2019
B2040

654

655 **Figure 5 (previous page): Anti-MAPK therapy affects signaling networks and transcriptomes**
656 **contingent on predictive mutations in organoids. A** Workflow of the experiment. In short, organoids
657 were treated for 48h with inhibitors, before disaggregation into single cells for CyTOF and scRNA-seq
658 analysis. For scRNA-seq, organoids were labelled for 2h with 4sU. **B** Schematic representation of
659 signaling network and transcriptional signatures associated with phenotypes or signaling pathways, as
660 indicated. **C** Heatmap of key CyTOF data. Average activities of selected analytes are given as log fold-
661 change after normalization to DMSO control condition. Range of color scale was adjusted for each
662 analyte. For relative changes between all analytes, see Supplementary Fig. 10). **D** Heatmap of key
663 scRNA seq data. Average activities of selected gene signatures are given as log fold-change after
664 normalization to DMSO control condition. Range of color scale was adjusted for each signature. **E**
665 Correlation between and within the CyTOF and scRNAseq data sets. For each line, average protein
666 analyte (CyTOF) or transcriptional signature (scRNA seq) values were plotted for all six experimental
667 conditions. Graphs give trend line and confidence intervals. **F** Upregulation of MAPK and YAP target
668 genes in mouse intestinal organoids after induction of oncogenic BRAF. Wnt target genes is not
669 significantly affected. For experimental details, see Riemer *et al.* (2015).

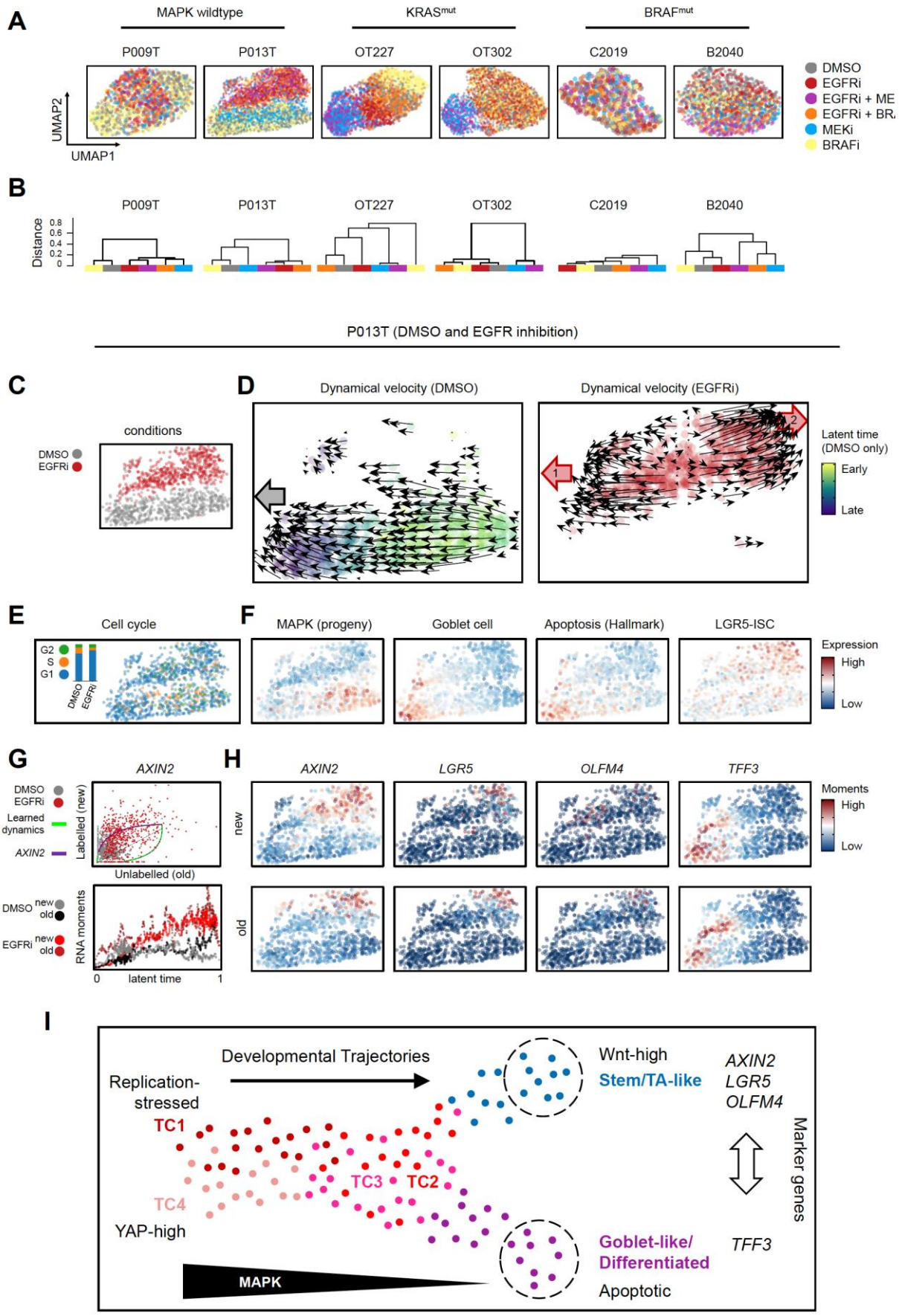
A
MAPK wildtype
KRASmut
BRAFmut
P009T
P013T
OT227
OT302
C2019
B2040
UMAP2
UMAP1
DMSO
EGFRi
EGFRi + ME
EGFRi + BR
MEKi
BRAFi
B
Distance
P013T (DMSO and EGFR inhibition)
C
conditions
DMSO
EGFRi
D
Dynamical velocity (DMSO)
Dynamical velocity (EGFRi)
Latent time (DMSO only)
Early
Late
E
Cell cycle
G2
S
G1
F
MAPK (progeny)
Goblet cell
Apoptosis (Hallmark)
LGR5-ISC
Expression
High
Low
G
AXIN2
Learned dynamics
Labelled (new)
Unlabelled (old)
RNA moments
latent time
H
LGR5
OLFM4
TFF3
new
old
Moments
I
Developmental Trajectories
Replication-stressed
TC1
TC4
YAP-high
TC3
TC2
MAPK
Wnt-high
Stem/TA-like
Goblet-like/ Differentiated
Apoptotic
Marker genes

672 **Figure 6 (previous page): Anti-MAPK therapy re-routes developmental trajectories in CRC organoids.**
673 **A** UMAPs of organoid single cell transcriptomes, color coded by treatment conditions, as indicated. **B**
674 Dendrograms of transcriptome similarities across treatment conditions, per organoid line. Height of
675 dendrogram represents is obtained by hierarchical clustering on the overlap of KNN neighborhoods
676 across conditions. (for details, see Methods). **C-H** Gene expression and RNA velocity analysis of P013T
677 organoids under DMSO and EGFR inhibitor conditions. **C** UMAPs of the two conditions, color coded by
678 condition **D** Developmental trajectories of organoid cells in the DMSO and EGFR treatment condition,
679 as determined by RNA velocity. Grey arrow indicates endpoint of DMSO condition. Red arrows indicate
680 the two endpoints of developmental trajectories after EGFR inhibition. DMSO cells are color coded by
681 latent time. Latent time cannot be defined for EGFR inhibited cells showing divergent trajectories **E**, **F**,
682 **H** UMAPs of the two conditions, color coded by cell cycle phase, activities of selected gene expression
683 signatures, or gene-specific expression moments, respectively. **G** Phase plot and latent time RNA
684 moments for *AXIN2* **I** Model of prototypical CRC cell trajectories.

685

686 **Extended View Figures**

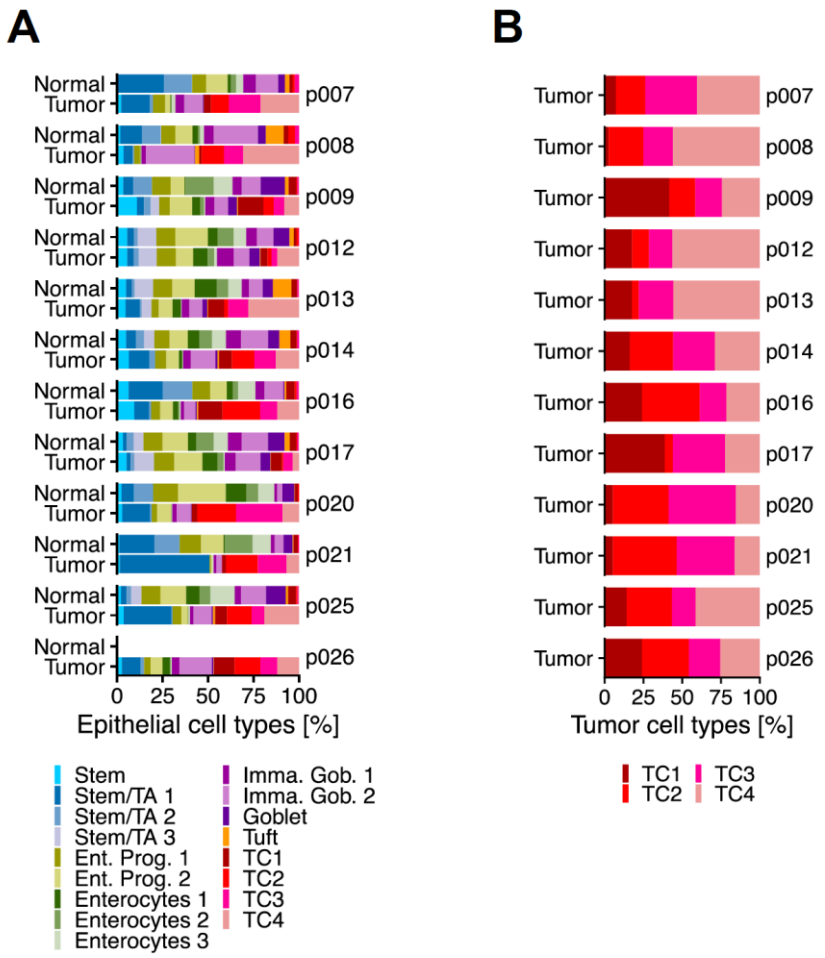

687

688 **Figure EV1: Cell type census, per patient. A** Relative prevalence of cells in the epithelial compartment,

689 per patient **B** Relative prevalence of TC1-4 cluster cells, per patient.

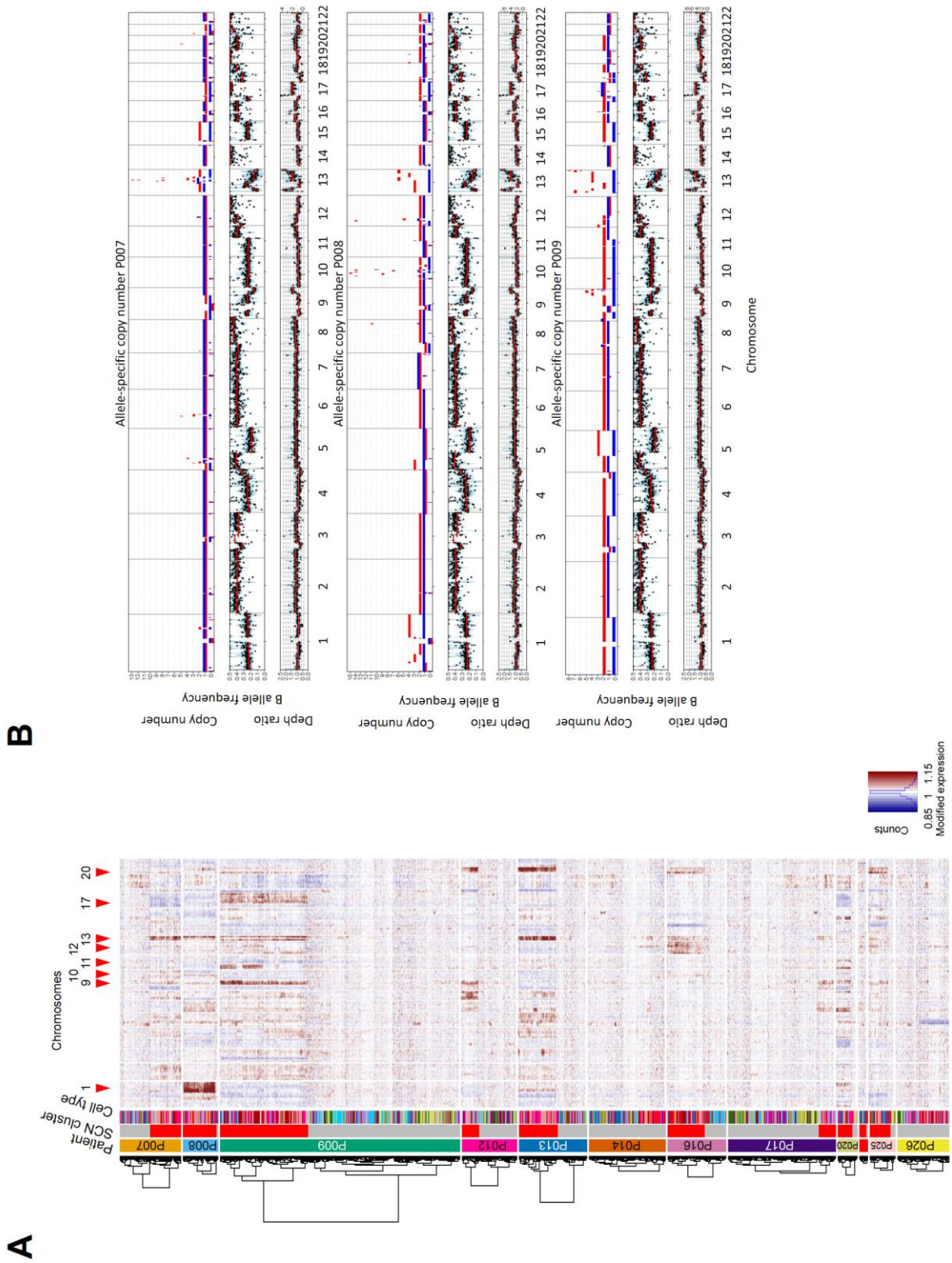

690

691 **Figure EV2: Assessment of copy-number variations. A** Copy-number calling from single cell
692 transcriptomes, using InferCNV. **B** Copy-number calling from exome sequences. To validate SCNAs
693 from single cell transcriptome data, we performed allele-specific SCNA calling for patients P007, P008
694 and P009 from bulk whole exome data. Germline variants were discovered *de novo* and read counts
695 were accumulated for each allele at heterozygous germline variants using bcftools v1.9 multi-allelic

696 caller. Discovered variants and read counts were passed to Sequenza 3.0 for segmentation and calling
697 of allele specific SCNAs. Top tracks: copy number segments of major and minor alleles. Middle tracks:
698 B (minor) allele frequency. Bottom tracks: depth ratio of matched tumor versus normal samples with
699 corresponding second axis of inferred copy number. P007 showed multiple LOH events on
700 chromosomes 1, 3, 5, 6, 8, 9, 13, 15, 17 and 21 as well as a focal amplification on chromosome 13.
701 P008 demonstrated a similar SCNA pattern with LOH events on chromosomes 8, 9, 10, 12, 13, 17 and
702 22 as well as multiple focal amplifications on chromosomes 8, 10, 12 and 13. P009 was characterized
703 by widespread copy-number neutral LOH in about 50% of the genome. Focal amplifications were found
704 on chromosomes 9 and 13.

705

706

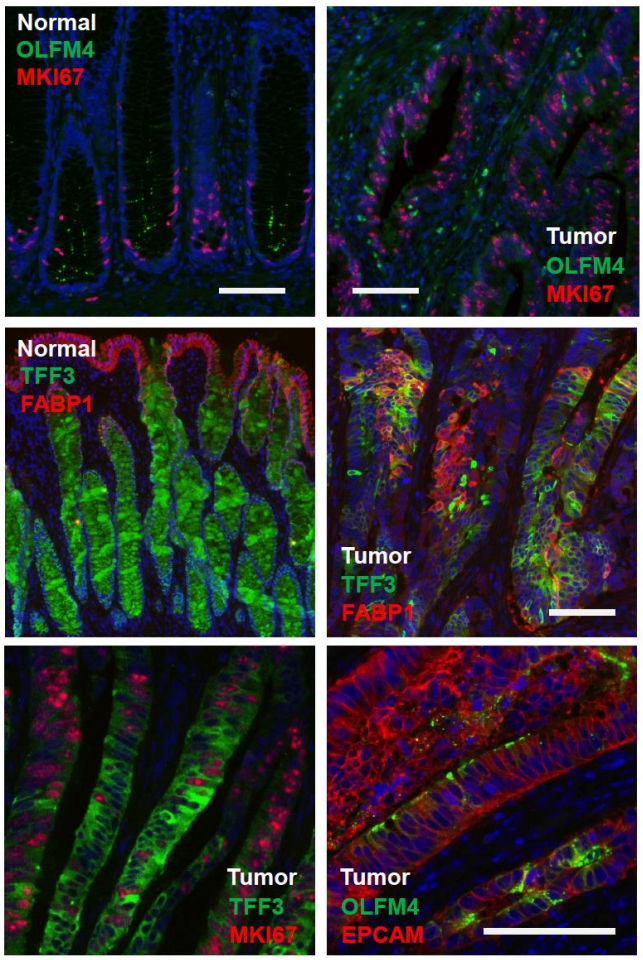

707

708 **Figure EV3: Assessment of CRC cell heterogeneity by immunofluorescence.** Immunofluorescence
709 analysis for OLFM4, MKI67, FABP1, and TFF3 in normal and tumor tissue. All sections are from patient
710 P009, except the EPCAM/OLFM4 co-staining that was done on tumor tissue of P016. Scale bars indicate
711 100µm. For marker expression in UMAP space, see Supplementary Fig. 3, above.

712

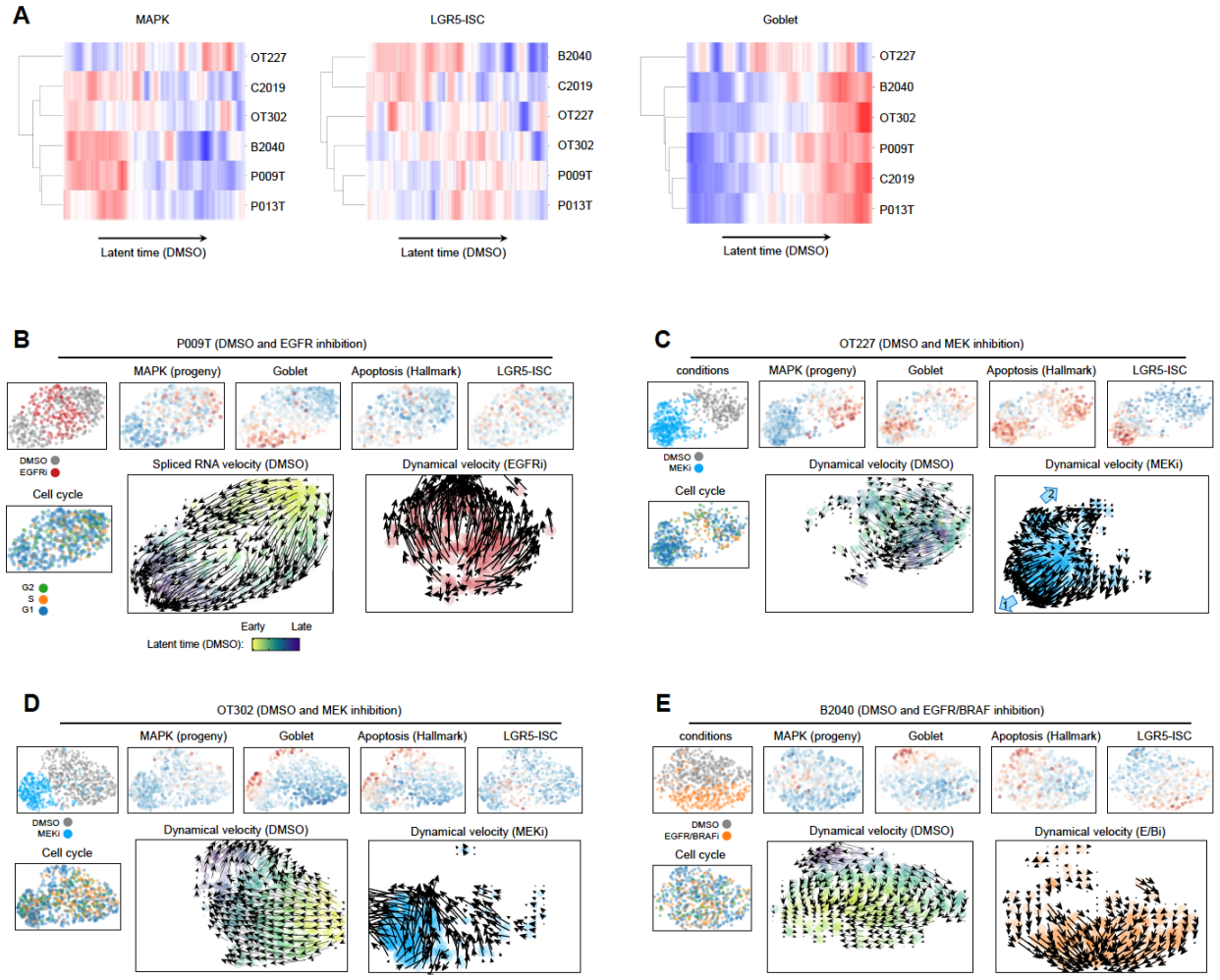

Figure EV4: Analysis of latent time and RNA velocity in CRC organoids. A Strength of MAPK, LGR5-ISC and Goblet-related signature gene expression along latent time, per line in control conditions (that is, without anti-MAPK treatment). No uniform trajectories could be called for OT227, resulting in random latent time. **B** Gene expression and RNA velocity analysis of P009T organoids under DMSO and EGFR inhibitor conditions. For this line, calling of RNA velocities ran in opposite directions for dynamical RNA velocity based on SLAM information, and for classical steady-state velocity by splicing. Only the latter velocity was in agreement with latent time. Based on analysis of phase plots, we propose that latent time and splicing-based RNA velocity are correct and represent the underlying biology, while SLAM velocity models may be confounded by genes displaying a OFF dynamic in disagreement with latent time. **C-D** Gene expression and RNA velocity analysis of OT227 and OT302 organoids under DMSO and MEK inhibitor conditions. **E** Gene expression and RNA velocity analysis of B2040 organoids under DMSO and combined EGFR/BRAF inhibitor conditions.

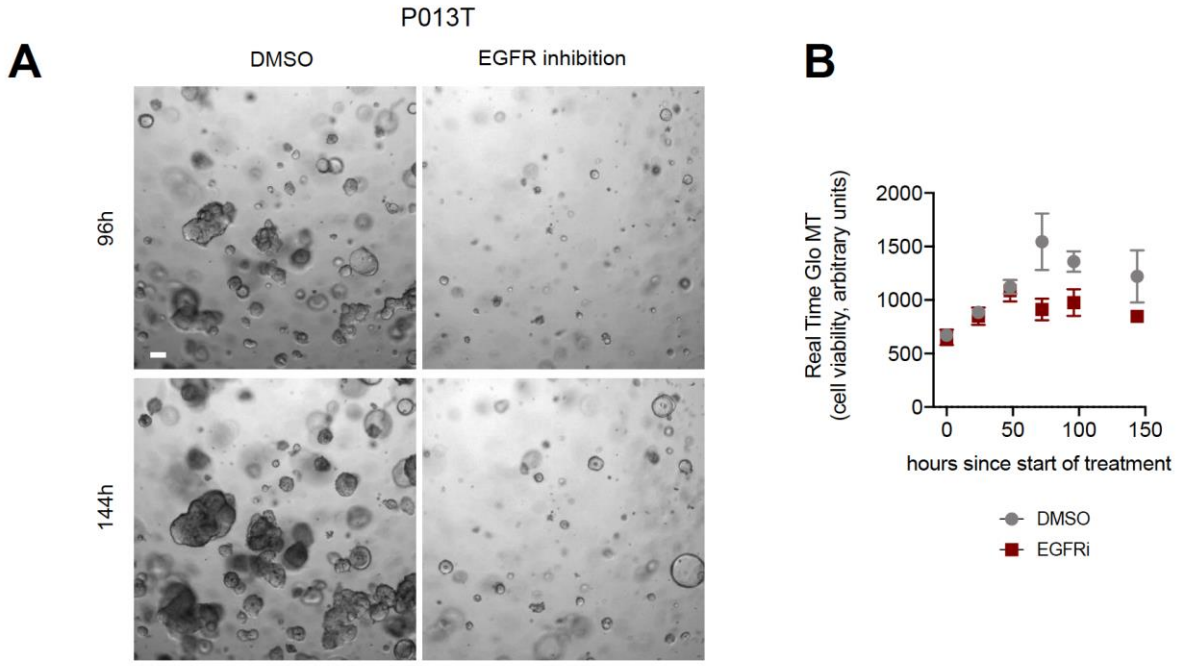

727

728 **Figure EV5: Long-term organoid culture of P013T reveals outgrowth of EGFR-resistant cells. A**
729 Phenotypes of DMSO control and EGFR-treated P013T cultures after 96 and 144h, as indicated.
730 Organoids growing under EGFR inhibition show a distinct spheroidal phenotype. **B** Metabolic cell
731 viability assays of triplicate DMSO control and EGFR inhibitor treated P013T cultures.

732

733 **References**

734 Adam M, Potter AS & Potter SS (2017) Psychrophilic proteases dramatically reduce single-cell RNA-
735 seq artifacts: A molecular atlas of kidney development. *Dev* 144: 3625–3632

736 Amado RG, Wolf M, Peeters M, Van Cutsem E, Siena S, Freeman DJ, Juan T, Sikorski R, Suggs S,
737 Radinsky R, *et al* (2008) Wild-type KRAS is required for panitumumab efficacy in patients with
738 metastatic colorectal cancer. *J Clin Oncol* 26: 1626–1634

739 Bergen V, Lange M, Peidli S, Wolf FA & Theis FJ (2020) Generalizing RNA velocity to transient cell
740 states through dynamical modeling. *Nat Biotechnol* 38: 1408–1414

741 Brabletz T, Jung A, Dag S, Hlubek F & Kirchner T (1999) β-catenin regulates the expression of the
742 matrix metalloproteinase-7 in human colorectal cancer. *Am J Pathol* 155: 1033–1038

743 Brandt R, Sell T, Lüthen M, Uhlitz F, Klinger B, Riemer P, Giesecke-Thiel C, Schulze S, El-Shimy IA,
744 Kunkel D, *et al* (2019) Cell type-dependent differential activation of ERK by oncogenic KRAS in
745 colon cancer and intestinal epithelium. *Nat Commun* 10: 2919

746 Buczacki SJA, Zecchini HI, Nicholson AM, Russell R, Vermeulen L, Kemp R & Winton DJ (2013)
747 Intestinal label-retaining cells are secretory precursors expressing Lgr5. *Nature* 495: 65–69

748 Chevrier S, Crowell HL, Zanotelli VRT, Engler S, Robinson MD & Bodenmiller B (2018) Compensation
749 of Signal Spillover in Suspension and Imaging Mass Cytometry. *Cell Syst* 6: 612–620

750 Corcoran RB, Andre T, Atreya CE, Schellens JHM, Yoshino T, Bendell JC, Hollebecque A, McRee AJ,
751 Siena S, Middleton G, *et al* (2018) Research article combined BRAF, EGFR, and MEK inhibition in
752 patients with BRAF V600E -mutant colorectal cancer. *Cancer Discov* 8: 428–443

753 Van Cutsem E, Köhne C-H, Hitre E, Zaluski J, Chang Chien C-R, Makhson A, D'Haens G, Pintér T, Lim R,
754 Bodoky G, *et al* (2009) Cetuximab and chemotherapy as initial treatment for metastatic
755 colorectal cancer. *N Engl J Med* 360: 1408–1417

756 Döring A, Weese D, Rausch T & Reinert K (2008) SeqAn An efficient, generic C++ library for sequence
757 analysis. *BMC Bioinformatics* 9: 11

758 Fearon ER (2011) Molecular genetics of colorectal cancer. *Annu Rev Pathol* 6: 479–507

759 Francescangeli F, Contavalli P, De Angelis ML, Careccia S, Signore M, Haas TL, Salaris F, Baiocchi M,
760 Boe A, Giuliani A, *et al* (2020) A pre-existing population of ZEB2+ quiescent cells with stemness
761 and mesenchymal features dictate chemoresistance in colorectal cancer. *J Exp Clin Cancer Res*
762 39

763 Fritsche-Guenther R, Witzel F, Sieber A, Herr R, Schmidt N, Braun S, Brummer T, Sers C & Blüthgen N
764 (2011) Strong negative feedback from Erk to Raf confers robustness to MAPK signalling. *Mol*
765 *Syst Biol* 7: 489

766 Goto N, Fukuda A, Yamaga Y, Yoshikawa T, Maruno T, Maekawa H, Inamoto S, Kawada K, Sakai Y,
767 Miyoshi H, *et al* (2019) Lineage tracing and targeting of IL17RB+ tuft cell-like human colorectal
768 cancer stem cells. *Proc Natl Acad Sci U S A* 116: 12996–13005

769 Guinney J, Dienstmann R, Wang X, de Reyniès A, Schlicker A, Soneson C, Marisa L, Roepman P,
770 Nyamundanda G, Angelino P, *et al* (2015) The consensus molecular subtypes of colorectal
771 cancer. *Nat Med* 21: 1350–1356

772 Hanahan D & Weinberg RA (2011) Hallmarks of cancer: the next generation. *Cell* 144: 646–674

773 Hatzivassiliou G, Song K, Yen I, Brandhuber BJ, Anderson DJ, Alvarado R, Ludlam MJC, Stokoe D, Gloor
774 SL, Vigers G, *et al* (2010) RAF inhibitors prime wild-type RAF to activate the MAPK pathway and
775 enhance growth. *Nature* 464: 431–435

776 Van Der Heijden M, Miedema DM, Waclaw B, Veenstra VL, Lecca MC, Nijman LE, Van Dijk E, Van
777 Neerven SM, Lodestijn SC, Lenos KJ, *et al* (2019) Spatiotemporal regulation of clonogenicity in
778 colorectal cancer xenografts. *Proc Natl Acad Sci U S A* 116: 6140–6145

779 Herzog VA, Reichholf B, Neumann T, Rescheneder P, Bhat P, Burkard TR, Wlotzka W, Von Haeseler A,
780 Zuber J & Ameres SL (2017) Thiol-linked alkylation of RNA to assess expression dynamics. *Nat*
781 *Methods* 14: 1198–1204

782 Jadhav U, Saxena M, O'Neill NK, Saadatpour A, Yuan GC, Herbert Z, Murata K & Shivdasani RA (2017)
783 Dynamic Reorganization of Chromatin Accessibility Signatures during Dedifferentiation of
784 Secretory Precursors into Lgr5+ Intestinal Stem Cells. *Cell Stem Cell* 21: 65–77

785 James KR, Gomes T, Elmentaite R, Kumar N, Gulliver EL, King HW, Stares MD, Bareham BR, Ferdinand
786 JR, Petrova VN, *et al* (2020) Distinct microbial and immune niches of the human colon. *Nat*
787 *Immunol* 21: 343–353

788 Jürges C, Dölken L & Erhard F (2018) Dissecting newly transcribed and old RNA using GRAND-SLAM.
789 *Bioinformatics* 34: i218–i226

790 Karapetis CS, Khambata-Ford S, Jonker DJ, O'Callaghan CJ, Tu D, Tebbutt NC, Simes RJ, Chalchal H,
791 Shapiro JD, Robitaille S, *et al* (2008) K-ras Mutations and Benefit from Cetuximab in Advanced
792 Colorectal Cancer. *N Engl J Med* 359: 1757–1765

793 Klotz-Noack K, Klinger B, Rivera M, Bublitz N, Uhlitz F, Riemer P, Lüthen M, Sell T, Kasack K, Gastl B, *et*

794 *al* (2020) SFPQ Depletion Is Synthetically Lethal with BRAFV600E in Colorectal Cancer Cells. *Cell*
795 *Rep* 32: 108184

796 Kopetz S, Grothey A, Yaeger R, Van Cutsem E, Desai J, Yoshino T, Wasan H, Ciardiello F, Loupakis F,
797 Hong YS, *et al* (2019) Encorafenib, binimetinib, and cetuximab in BRAF V600E–mutated
798 colorectal cancer. *N Engl J Med* 381: 1632–1643

799 Köster J & Rahmann S (2012) Snakemake-a scalable bioinformatics workflow engine. *Bioinformatics*
800 28: 2520–2522

801 Kowalczyk MS, Tirosh I, Heckl D, Rao TN, Dixit A, Haas BJ, Schneider RK, Wagers AJ, Ebert BL & Regev
802 A (2015) Single-cell RNA-seq reveals changes in cell cycle and differentiation programs upon
803 aging of hematopoietic stem cells. *Genome Res* 25: 1860–1872

804 Kreso A & Dick JE (2014) Evolution of the cancer stem cell model. *Cell Stem Cell* 14: 275–291

805 Lamprecht S, Schmidt EM, Blaj C, Hermeking H, Jung A, Kirchner T & Horst D (2017) Multicolor
806 lineage tracing reveals clonal architecture and dynamics in colon cancer. *Nat Commun* 8: 1406

807 Lasry A, Zinger A & Ben-Neriah Y (2016) Inflammatory networks underlying colorectal cancer. *Nat*
808 *Immunol* 17: 230–240

809 Lee HO, Hong Y, Etlioglu HE, Cho YB, Pomella V, Van den Bosch B, Vanhecke J, Verbandt S, Hong H,
810 Min JW, *et al* (2020) Lineage-dependent gene expression programs influence the immune
811 landscape of colorectal cancer. *Nat Genet* 52: 594–603

812 Liberzon A, Birger C, Thorvaldsdóttir H, Ghandi M, Mesirov JP & Tamayo P (2015) The Molecular
813 Signatures Database Hallmark Gene Set Collection. *Cell Syst* 1: 417–425

814 Mamlouk S, Childs LH, Aust D, Heim D, Melching F, Oliveira C, Wolf T, Durek P, Schumacher D, Bläker
815 H, *et al* (2017) DNA copy number changes define spatial patterns of heterogeneity in colorectal
816 cancer. *Nat Commun* 8: 14093

817 La Manno G, Soldatov R, Zeisel A, Braun E, Hochgerner H, Petukhov V, Lidschreiber K, Kastriti ME,
818 Lönnerberg P, Furlan A, *et al* (2018) RNA velocity of single cells. *Nature* 560: 494–498

819 McInnes L, Healy J, Saul N & Großberger L (2018) UMAP: Uniform Manifold Approximation and
820 Projection. *J Open Source Softw* 3: 861

821 Merlos-Suárez A, Barriga FM, Jung P, Iglesias M, Céspedes MV, Rossell D, Sevillano M, Hernando-
822 Momblona X, da Silva-Diz V, Muñoz P, *et al* (2011) The intestinal stem cell signature identifies
823 colorectal cancer stem cells and predicts disease relapse. *Cell Stem Cell* 8: 511–524

824 Misale S, Di Nicolantonio F, Sartore-Bianchi A, Siena S & Bardelli A (2014) Resistance to Anti-EGFR
825 therapy in colorectal cancer: From heterogeneity to convergent evolution. *Cancer Discov* 4:
826 1269–1280

827 Morral C, Stanisavljevic J, Hernando-Momblona X, Mereu E, Álvarez-Varela A, Cortina C, Stork D,
828 Slebe F, Turon G, Whissell G, *et al* (2020) Zonation of Ribosomal DNA Transcription Defines a
829 Stem Cell Hierarchy in Colorectal Cancer. *Cell Stem Cell* 26: 845–861

830 Muñoz J, Stange DE, Schepers AG, van de Wetering M, Koo B-K, Itzkovitz S, Volckmann R, Kung KS,
831 Koster J, Radulescu S, *et al* (2012) The Lgr5 intestinal stem cell signature: robust expression of
832 proposed quiescent '+4' cell markers. *EMBO J* 31: 3079–3091

833 O'Brien CA, Pollett A, Gallinger S, Dick JE, O'Brien CA, Pollett A, Gallinger S & Dick JE (2007) A human
834 colon cancer cell capable of initiating tumour growth in immunodeficient mice. *Nature* 445:
835 106–110

836 De Palma FDE, D'argenio V, Pol J, Kroemer G, Maiuri MC & Salvatore F (2019) The molecular
837 hallmarks of the serrated pathway in colorectal cancer. *Cancers (Basel)* 11: 1017

838 Parikh K, Antanaviciute A, Fawkner-Corbett D, Jagielowicz M, Aulicino A, Lagerholm C, Davis S,
839 Kinchen J, Chen HH, Alham NK, *et al* (2019) Colonic epithelial cell diversity in health and
840 inflammatory bowel disease. *Nature* 567: 49–55

841 Rajewsky N, Almouzni G, Gorski SA, Aerts S, Amit I, Bertero MG, Bock C, Bredenoord AL, Cavalli G,
842 Chiocca S, *et al* (2020) LifeTime and improving European healthcare through cell-based
843 interceptive medicine. *Nature* 587: 377–386

844 Ricci-Vitiani L, Lombardi DG, Pilozzi E, Biffoni M, Todaro M, Peschle C & De Maria R (2007)
845 Identification and expansion of human colon-cancer-initiating cells. *Nature* 445: 111–115

846 Riemer P, Sreekumar A, Reinke S, Rad R, Schäfer R, Sers C, Bläker H, Herrmann BG & Morkel M (2015)
847 Transgenic expression of oncogenic BRAF induces loss of stem cells in the mouse intestine,
848 which is antagonized by β-catenin activity. *Oncogene* 34: 3164–3175

849 Sato T, Stange DE, Ferrante M, Vries RGJ, van Es JH, van den Brink S, Van Houdt WJ, Pronk A, Van
850 Gorp J, Siersema PD, *et al* (2011) Long-term expansion of epithelial organoids from human
851 colon, adenoma, adenocarcinoma, and Barrett's epithelium. *Gastroenterology* 141: 1762–1772

852 Schubert M, Klinger B, Klünemann M, Sieber A, Uhlitz F, Sauer S, Garnett MJ, Blüthgen N & Saez-
853 Rodriguez J (2018) Perturbation-response genes reveal signaling footprints in cancer gene
854 expression. *Nat Commun* 9: 20

855 Schütte M, Risch T, Abdavi-Azar N, Boehnke K, Schumacher D, Keil M, Yildiriman R, Jandrasits C,
856 Borodina T, Amstislavskiy V, *et al* (2017) Molecular dissection of colorectal cancer in pre-clinical
857 models identifies biomarkers predicting sensitivity to EGFR inhibitors. *Nat Commun* 8: 14262

858 Schwitalla S, Fingerle AA, Cammareri P, Nebelsiek T, Göktuna SI, Ziegler PK, Canli O, Heijmans J, Huels
859 DJ, Moreaux G, *et al* (2013) Intestinal Tumorigenesis Initiated by Dedifferentiation and
860 Acquisition of Stem-Cell-like Properties. *Cell* 152: 25–38

861 Serra D, Mayr U, Boni A, Lukonin I, Rempfler M, Challet Meylan L, Stadler MB, Strnad P, Papasaikas P,
862 Vischi D, *et al* (2019) Self-organization and symmetry breaking in intestinal organoid
863 development. *Nature* 569: 66–72

864 Sheu JJ-C, Guan B, Tsai F-J, Hsiao EY-T, Chen C-M, Seruca R, Wang T-L & Shih I-M (2012) Mutant BRAF
865 Induces DNA Strand Breaks, Activates DNA Damage Response Pathway, and Up-Regulates
866 Glucose Transporter-1 in Nontransformed Epithelial Cells. *Am J Pathol* 180: 1179–1188

867 Shimokawa M, Ohta Y, Nishikori S, Matano M, Takano A, Fujii M, Date S, Sugimoto S, Kanai T & Sato T
868 (2017) Visualization and targeting of LGR5+ human colon cancer stem cells. *Nature* 545: 187–
869 192

870 Smillie CS, Biton M, Ordovas-Montanes J, Sullivan KM, Burgin G, Graham DB, Herbst RH, Rogel N,
871 Slyper M, Waldman J, *et al* (2019) Intra- and Inter-cellular Rewiring of the Human Colon during
872 Ulcerative Colitis. *Cell* 178: 714-730.e22

873 Stuart T, Butler A, Hoffman P, Hafemeister C, Papalexi E, Mauck WM, Hao Y, Stoeckius M, Smibert P
874 & Satija R (2019) Comprehensive Integration of Single-Cell Data. *Cell* 177: 1888-1902.e21

875 Sun C, Fang Y, Labrie M, Li X & Mills GB (2020) Systems approach to rational combination therapy:
876 PARP inhibitors. *Biochem Soc Trans* 48: 1101–1108

877 Tong K, Pellón-Cárdenas O, Sirihorachai VR, Warder BN, Kothari OA, Perekatt AO, Fokas EE, Fullem
878 RL, Zhou A, Thackray JK, *et al* (2017) Degree of Tissue Differentiation Dictates Susceptibility to
879 BRAF-Driven Colorectal Cancer. *Cell Rep* 21: 3833–3845

880 Vermeulen L, De Sousa E Melo F, van der Heijden M, Cameron K, de Jong JH, Borovski T, Tuynman JB,
881 Todaro M, Merz C, Rodermond H, *et al* (2010) Wnt activity defines colon cancer stem cells and
882 is regulated by the microenvironment. *Nat Cell Biol* 12: 468–476

883 van de Wetering M, Sancho E, Verweij C, de Lau W, Oving I, Hurlstone A, van der Horn K, Batlle E,
884 Coudreuse D, Haramis AP, *et al* (2002) The beta-catenin/TCF-4 complex imposes a crypt
885 progenitor phenotype on colorectal cancer cells. *Cell* 111: 241–250

886 Wolf FA, Angerer P & Theis FJ (2018) SCANPY: large-scale single-cell gene expression data analysis.
887 *Genome Biol* 19: 15

888 Woolston A, Khan K, Spain G, Barber LJ, Griffiths B, Gonzalez-Exposito R, Hornsteiner L, Punta M, Patil
889 Y, Newey A, *et al* (2019) Genomic and Transcriptomic Determinants of Therapy Resistance and
890 Immune Landscape Evolution during Anti-EGFR Treatment in Colorectal Cancer. *Cancer Cell* 36:
891 35-50.e9

892 Zanconato F, Cordenonsi M & Piccolo S (2016) YAP/TAZ at the Roots of Cancer. *Cancer Cell* 29: 783–
893 803

894 Zhan T, Ambrosi G, Wandmacher AM, Rauscher B, Betge J, Rindtorff N, Häussler RS, Hinsenkamp I,
895 Bamberg L, Hessling B, *et al* (2019) MEK inhibitors activate Wnt signalling and induce stem cell
896 plasticity in colorectal cancer. *Nat Commun* 10: 2197

897 Zhang L, Li Z, Skrzypczynska KM, Fang Q, Zhang W, O'Brien SA, He Y, Wang L, Zhang Q, Kim A, *et al*
898 (2020) Single-Cell Analyses Inform Mechanisms of Myeloid-Targeted Therapies in Colon Cancer.
899 *Cell* 181: 442-459.e29

900